Manuscript-Revision 2

Fingerprinting REE mineralization and hydrothermal remobilization history of the Carbonatite-Alkaline complexes, Central China: Constraints from *in situ* elemental and isotopic analyses of phosphate minerals

Jian-Hui Su[1], Xin-Fu Zhao[1*], Xiao-Chun Li[2, 3], Zhi-Kun Su[1], Rui Liu[1], Zhi-Jun Qin[4], Mi Chen[4]

[1] State Key Laboratory of Geological Processes and Mineral Resources, and School of Earth Resources, China University of Geosciences, Wuhan 430074, China

[2] Key Laboratory of Mineral Resources, Institute of Geology and Geophysics, Chinese Academy of Sciences, Beijing 100029, China

[3]College of Earth and Planetary Sciences, University of Chinese Academy of Sciences, Beijing 100049, China

[4] Geological Survey of Hubei Province, Wuhan 430034, China

*Corresponding author: xfzhao@cug.edu.cn

Abstract

Carbonatites and related alkaline rocks host most REE resources. Phosphate minerals, e.g., apatite and monazite, commonly occur as the main REE-host in carbonatites and have been used for tracing magmatic and mineralization processes. Many carbonatite intrusions undergo metamorphic and/or metasomatic modification after emplacement; however, the effects of such secondary events are controversial. In this study, the Miaoya and Shaxiongdong carbonatite-alkaline complexes, in the South Qinling Belt of Central China, are selected to unravel their magmatic and hydrothermal remobilization histories. Both the complexes are accompanied by Nb-REE mineralization and contain apatite and monazite-(Ce) as the major REE carriers.

Apatite grains from the two complexes commonly show typical replacement textures related to fluid metasomatism, due to coupled dissolution-reprecipitation. The altered apatite domains, which contain abundant monazite-(Ce) inclusions or are locally surrounded by fine-grained monazite-(Ce), have average REE concentrations lower than primary apatite. These monazite-(Ce) inclusions and fine-grained monazite-(Ce) grains are proposed to have formed by the leaching REE from primary apatite grains during fluid metasomatism. A second type of monazite-(Ce), not spatially associated with apatite, shows porous textures and zoning under BSE imaging. Spot analyses of these monazite-(Ce) grains have variable U-Th-Pb ages of 210-410 Ma and show a peak age of 230 Ma, which is significantly younger than the emplacement age (440-430 Ma) but are

roughly synchronous with a regionally metamorphic event related to the collision between the North China Craton and Yangtze Block along the Mianlue suture. However, *in situ* LA-MC-ICP-MS analyses of those grains show that they have initial Nd values same as those of magmatic apatite and whole rock. We suggest these monazite-(Ce) grains crystallized from the early Silurian carbonatites and have been partially or fully modified during a Triassic metamorphic event, partially resetting U-Pb ages over a wide range. Mass-balance calculations, based on mass proportions and the REE contents of monazite-(Ce) and apatite, demonstrate that the quantity of metasomatized early Silurian monazite-(Ce) is far higher than the proportion of monazite-(Ce) resulting from the metasomatic alteration of the apatite. Therefore, Triassic metamorphic events largely reset the U-Th-Pb isotopic system of the primary monazite-(Ce) and apatite, but only had limited or local effects on REE remobilization in the carbonatite-alkaline complexes in the South Qinling Belt. Such scenarios may be widely applicable for other carbonatite and hydrothermal systems.

Keywords: Carbonatite-alkaline complex, Phosphate minerals, REE mineralization, *in situ* isotopic analyses, Metasomatic alteration

Introduction

Global demand for rare earth elements (REE) has been continuously increasing during the past decades because of their critical roles in modern industries (Weng et al. 2015; Goodenough et al. 2017; Zhou et al. 2017). These elements are mainly sourced from carbonatites and related alkaline complexes (Chakhmouradian and Wall, 2012; Goodenough et al. 2017; Zhou et al. 2017), and hence REE enrichment and mineralization processes in carbonatites have attracted wide interest in recent years (e.g., Verplanck et al. 2016; Simandl and Paradis, 2018). Phosphate minerals, e.g., apatite and monazite, commonly occur as the main REE-carriers in carbonatite systems, and can also accommodate a range of other trace elements (e.g., Th and U) (e.g., Mao et al. 2016; Chen et al. 2017), making them ideal proxies for *in situ* elemental and isotopic analyses. Therefore, they have been commonly used for tracing the source, evolution, and mineralization processes of carbonatite systems (e.g., Le Bas, 1979; Buhn et al. 2001; Broom-Fendley et al. 2016; Zi et al. 2017; Song et al. 2018).

Apatite is known to crystallize throughout the fractionation process of carbonatites (Gittins, 1989), and can hence be a good mineral recorder of magma evolution (Bühn, 2001; Wang et al. 2014). However, it has been documented that apatite can be altered by hydrothermal fluids, through the process of coupled dissolution-reprecipitation (Putnis, 2002, 2009; Harlov et al. 2003, 2005, 2015), forming new REE phases, such as monazite

78 (Broom-Fendley et al. 2016, 2017). Therefore, metasomatic alteration of apatite may be
79 an important mechanism for REE enrichment in carbonatites.

80 Monazite has been widely used as a U-Th-Pb geochronometer in carbonatites (e.g.,
81 Poletti et al. 2016; Zi et al. 2017; Song et al. 2018). However, monazite sometimes yields
82 ages significantly younger than zircon U-Th-Pb dating, which can lead to different
83 interpretations for age discrepancies (e.g., Millonig et al. 2013; Downes et al. 2016;
84 Slezak and Spandler, 2019). In most cases, the younger monazite ages are synchronous
85 with regionally tectonothermal events and hence have been suggested as a late stage
86 tectonothermal overprint (Catlos et al. 2008; Millonig et al. 2012; Ling et al. 2013;
87 Downes et al. 2016; Kim et al. 2016; Zi et al. 2017; Slezak and Spandler, 2019). Recently,
88 these younger monazites have been further interpreted as the products of metasomatic
89 alteration of the primary apatite (Catlos et al. 2008; Ying et al. 2017; Zi et al. 2017;
90 Zhang et al. 2019), indicating that REE remobilization may be significant during
91 post-magmatic events. Alternatively, younger monazite ages may result from the
92 disturbance of U-Th-Pb isotopic systems of primary monazite during tectonothermal
93 events (Millonig et al. 2013; Downes et al. 2016; Slezak and Spandler, 2019). Therefore,
94 the understanding of monazite U-Pb ages is essential for assessing the possible roles of
95 primary and secondary processes of REE enrichment history in carbonatite systems.

96 Recent advances in micro-analytical techniques have enabled us to determine
97 elemental and isotopic compositions on sub-grains of monazite and apatite (e.g., Xu et al.

2015; Engi, 2017), providing new insights into such processes. Two carbonatite-alkaline complexes with low-grade REE mineralization, the Miaoya and Shaxiongdong complex, South Qinling Belt of Central China, were selected to evaluate their REE mineralization histories in this study. Both complexes have zircon U-Pb ages of 440-430 Ma, which have been interpreted as intrusive ages (Xu et al. 2008; Ying et al. 2017; Zhu et al. 2017; Chen et al. 2018; Su et al. 2019). However, previous studies also reported monazite ages of ~230 Ma, which has been interpreted as either an independent REE mineralization (Xu et al. 2014) or an REE remobilization event (Ying et al. 2017; Zhang et al. 2019). Therefore, these carbonatite-alkaline complexes provide an excellent opportunity to test the two different mechanisms. This study presents detailed textural observations together with *in situ* elemental and U-Th-Pb and Nd isotopic analyses on phosphates (monazite-(Ce) and apatite), which are the main REE-carrying minerals in carbonatites. Our results unravel a complex crystallization and alteration history of REE minerals and provide significant constraints on the hydrothermal resetting of monazite U-Th-Pb isotopes during regional metamorphism. The conclusions may be widely applicable to other carbonatite and hydrothermal systems.

Geological background

The Miaoya and Shaxiongdong carbonatite-alkaline complexes are located within the Qinling Orogen, Central China. The Qinling Orogen consists of four tectonic belts, including the southern margin of the North China Craton, the North Qinling Belt, the

South Qinling Belt, and the northern margin of Yangtze Block from north to south (Fig. 1a). The four tectonic belts underwent complicated evolution histories before colliding during the early-middle Triassic. Here we focus on the tectonic evolution of the South Qinling Belt and adjacent areas where the Miaoya and Shaxiongdong carbonatite-alkaline complexes are located. More details on the tectonic setting can be referred to Wu and Zheng (2013) and Dong and Santosh (2016).

The South Qinling Belt consists of Neoarchean basement and Neoproterozoic clastic and volcanic rocks, overlain by Upper Sinian to Triassic sedimentary rocks that underwent greenschist facies metamorphism (Wu and Zheng, 2013; Dong and Santosh, 2016). Sinian to Ordovician sedimentary rocks include platform carbonate, shale, and sandstone. The Silurian to Devonian strata contain a 10 km thick sequence of metagraywacke, slate, phyllite, and marble, indicating large-scale subsidence of sedimentary basins and rapid sedimentation at the beginning of the Silurian (Gao et al. 1995). This implies an extensional tectonic setting in the northern part of the Yangtze Block during the Silurian to early Devonian (Wu and Zheng, 2013; Dong and Santosh, 2016). Silurian alkaline magmatism is widely reported in this region, including mafic-ultramafic dykes and basalts (Zhang et al. 2007; Wang et al. 2015), trachytes and syenites (Wang et al. 2017), and carbonatite-alkaline complexes (Xu et al. 2008; Zhu et al. 2017). These magmatic rocks are interpreted to result from middle Paleozoic rifting in the northern margin of the Yangtze Block. This rifting event is probably linked to the opening

of the Mianlue Ocean during the late Paleozoic (Wu and Zheng, 2013; Dong and Santosh, 2016). High-pressure blueschist rocks occur in the northern part of the South Qinling Belt, and have Ar-Ar phengite and riebeckite ages of ca. 216-236 Ma (Mattauer et al. 1985; Ratschbacher et al. 2003). They represent the final collision between the North China Craton and Yangtze Block along the Mianlue suture.

Geology of the Miaoya and Shaxiongdong Complexes

Among the early Silurian alkaline intrusions in the South Qinling Belt, the Miaoya and Shaxiongdong complexes contain Nb-REE mineralization (Xu et al. 2008; Ying et al. 2017; Zhu et al. 2017; Chen et al. 2018; Su et al. 2019). The Miaoya complex intrudes into early Silurian carbonaceous slate and weakly metamorphosed tuff in the northern part, and Precambrian sedimentary and volcanic rocks in the southern part (Fig. 1b). The complex consists of syenite, calcite carbonatite, and ankerite carbonatite (Fig. 1b; Fig. 2a-d). Syenite and calcite carbonatite host most of the Nb ores, and carbonatites contain most of the REE ores. The syenite consists mainly of K-feldspar, accompanied by zircon, Nb-bearing minerals (e.g., niobaeschynite and columbite), and Fe-Ti oxides. Calcite carbonatite consists mainly of calcite, accompanied by variable amounts of apatite and biotite (Fig. 2b-c), with accessory Fe-Ti oxides, columbite, and REE minerals (monazite-(Ce), allanite-(Ce), bastnäsite-(Ce), and parasite-(Ce)). Ankerite carbonatite is mainly composed of ankerite and calcite with accessory apatite, fluorite, monazite-(Ce), bastnäsite-(Ce), and parasite-(Ce).

158 The Shaxiongdong complex intruded into the Neoproterozoic meta-sedimentary and
159 volcanic rocks of the Wudang Group (Fig. 1c). The complex is composed of
160 meta-pyroxenite, syenite, and calcite carbonatite (Fig. 1c; Fig. 2e-g). Niobium
161 mineralized zones are associated with syenite and carbonatite. REE-bearing orebodies are
162 mainly hosted in carbonatite. Meta-pyroxenite consists of amphibole and chlorite, plus
163 variable amounts of epidote, albite, biotite, titanite, and pyroxene. Syenite is composed
164 mainly of albite and K-feldspar, with variable amounts of zircon, titanite, amphibole,
165 biotite, and epidote. Calcite carbonatite consists mainly of medium to coarse-grained
166 calcite, accompanied by variable amounts of apatite, aegirine, and biotite (Fig. 2g).
167 Accessory minerals in the carbonatite include monazite-(Ce), allanite-(Ce),
168 bastnäsite-(Ce), pyrochlore, barite, and Fe-Ti oxides.

169 In both the Miaoya and Shaxiongdong complexes, syenite samples may contain
170 abundant carbonate minerals associated with silicate minerals (biotite ± aegirine), minor
171 apatite, and REE minerals, which are interstitial to K-feldspar or occur as veinlets and
172 breccias (Fig. 2e). This type of syenite has been called a carbonated syenite by Su et al.
173 (2019). Carbonate phases within these samples have been inferred to crystallize from
174 carbonate melts evolved from carbonated alkali silicate melts.

175 **Sampling and analytical methods**

176 Thirteen samples, including carbonated syenite and calcite carbonatite, were selected
177 for *in situ* elemental and isotopic analyses from the Miaoya and Shaxiongdong complexes.
178 The main features of these samples are listed in Table 1.

179 Polished thin sections of each sample were investigated first by petrographic
180 microscope. Then, optical microscope cathodoluminescence (CL) images were obtained
181 using a Leica DM2700P microscope coupled with a CITL MK5-2 system, at the State
182 Key Laboratory of Geological Processes and Mineral Resources (GPMR), China
183 University of Geosciences (CUG), Wuhan, China. Representative monazite-(Ce) and
184 apatite grains were also observed under backscattered electron (BSE) imaging using a
185 JEOL JXA-8230 at the Center of Material Research and Analysis, Wuhan University of
186 Technology (WUT), Wuhan, China, prior to elemental and isotopic analysis.

187 Trace element analyses of apatite were performed using a GeolasPro laser ablation (LA)
188 system coupled to an Agilent 7700e type inductively coupled plasma-mass spectrometer
189 (ICP-MS) instrument at the GPMR, CUG. Detailed operating conditions for the laser
190 ablation system and the ICP-MS instrument and data reduction are as described in Zong
191 et al. (2017) and are summarized here. Helium was applied as carrier gas, while Ar was
192 used as the make-up gas and mixed with the carrier gas via a T-connect or before entering
193 the ICP. A "wire" signal smoothing device is included in this laser ablation system (Hu et
194 al. 2015). Analyses were performed using a beam diameter of 44 μm and a repetition rate
195 of 6 Hz. Trace element compositions of minerals were calibrated against various

196 reference materials (BHVO-2G, BCR-2G and BIR-1G) without using an internal standard
197 (Liu et al. 2008). Each analysis incorporated a background acquisition of approximately
198 20-30 s followed by 50 s of data acquisition from the sample. An Excel-based software
199 ICPMSDataCal was used to perform off-line selection and integration of background and
200 analyte signals, and time-drift correction and quantitative calibration for trace element
201 analysis (Liu et al. 2008).

202 U-Th-Pb dating of monazite-(Ce) was conducted by LA-ICP-MS at the GPMR, CUG,
203 Wuhan. Analyses were performed using a beam diameter of 16 μm and a repetition rate
204 of 2 Hz. Each analysis incorporated a background acquisition of approximately 20 to 30 s
205 followed by 50 s of data acquisition. Monazite standard 44069 was used as an external
206 standard for U-Th-Pb dating calibration. The analysis of monazite standard 44069 yielded
207 a weighted mean age of 424.6 ± 1.1 Ma, which is consistent with the recommended
208 ID-TIMS age of 424.9 ± 0.4 Ma (Aleinikoff et al. 2006). Off-line data selection and
209 integration were performed by using ICPMSDataCal software (Liu et al. 2008, 2010).
210 Concordia diagrams and weighted mean calculations were plotted by Isoplot/Ex_ver3
211 (Ludwig, 2003).

212 *In situ* monazite-(Ce) U-Th-Pb ages for sample 16MY-33 were also analyzed using the
213 SHRIMP II at the John de Laeter Centre, Curtin University, Australia. SHRIMP monazite
214 analytical procedures have been described and discussed in detail by Fletcher et al.
215 (2010). Monazite reference materials FRENCH, Z2234, and Z2908 in a separate mount

were analyzed concurrently for Pb/U and Pb/Th calibration, corrections for instrumental mass fractionation (IMF), and matrix effects required for variable U, Th, Y, and Nd contents (Fletcher et al. 2010). A primary beam of O_2^- ions was focused through a 30 or 50 μm Kohler aperture to produce an oval spot of ~10 μm, with a current intensity of 0.2–0.4 nA. The secondary ion system was focused through a 100 μm collector slit onto an electron multiplier to produce mass peaks with flat tops and a mass resolution (M/ΔM at 1% peak height) of > 5000 in all sessions. Data were collected in sets of eight scans, processed using Squid-2 software (Ludwig, 2009). Concordia diagrams and weighted mean calculations were made using Isoplot/Ex_ver3 (Ludwig, 2003).

Neodynium isotope ratios of apatite and monazite-(Ce) grains were measured by a Neptune Plus MC-ICP-MS (ThermoFisher Scientific, Bremen, Germany) in combination with a Geolas HD excimer ArFlaser ablation system (Coherent, Göttingen, Germany) at the GPMR, CUG. In the laser ablation system, He was used as the carrier gas within the ablation cell and was merged with Ar (makeup gas) after the ablation cell. Small amounts of nitrogen were added to the Ar make-up gas flow in order to improve the detector sensitivity for Nd isotopes (Xu et al. 2015). The analyses were conducted with a spot size of 60 or 90 μm and a repetition rate of 8 Hz for apatite, and a spot size of 24 μm, and a repetition rate 2 Hz for monazite. A new signal-smoothing device was used downstream from the sample cell to efficiently eliminate short-term variations in the signal and remove the Hg from the background and sample aerosol particles (Hu et al. 2015). The

Neptune Plus is equipped with nine Faraday cups fitted with $10^{11}\Omega$ resistors. Isotopes ^{142}Nd, ^{143}Nd, ^{144}Nd, ^{145}Nd, ^{146}Nd, ^{147}Sm, ^{148}Nd and ^{149}Sm were collected in Faraday cups using static mode. The mass discrimination factor for $^{143}Nd/^{144}Nd$ was determined using $^{146}Nd/^{144}Nd$ (0.7219) with the exponential law. The ^{149}Sm signal was used to correct the remaining ^{144}Sm interference on ^{144}Nd, using the $^{144}Sm/^{149}Sm$ ratio of 0.2301. The mass fractionation of $^{144}Sm/^{149}Sm$ was corrected by the $^{147}Sm/^{149}Sm$ normalization, using the $^{144}Sm/^{149}Sm$ ratio of 1.08680 and exponential law. Two natural apatite megacrysts, Durango and MAD, were used as the unknown samples to verify the accuracy of the calibration method for *in situ* Nd isotope analysis of apatites. A monazite standard, 44069, and a titanite standard, MKED1, were used as the unknown samples to verify the accuracy of the calibration for *in situ* Nd isotope analysis of the monazite. The chemical and Nd isotopic compositions of these standard samples have been reported by Xu et al. (2015) and Spandler et al. (2016).

Petrography of apatite and monazite-(Ce)

Apatite

Apatite occurs as euhedral to subhedral single crystal or aggregates in the carbonatites and carbonated syenites of the Miaoya and Shaxiongdong complexes (Fig. 3). It is either intergrown with calcite, biotite and aegirine, or enveloped by these minerals (Fig. 3a), implying that the apatite was an igneous product that crystallized from a carbonatite melt. Apatite grains from the two complexes show similar textures under CL and BSE imaging,

and can be classified into two types. The first type of apatite grains has a green core surrounded by an irregular rim of purple to blue (Fig. 3b, d) under CL imaging. The core-rim boundaries are transitional in the BSE images, implying a gradual growth zonation (Fig. 3c). The other type of apatite grains does not show obvious zoning and is purple to blue throughout (Fig. 3d-e). However, both types of apatite have been metasomatized by late-stage hydrothermal fluids that have resulted in dark domains under BSE imaging, corresponding to the greenish color in CL images (Fig. 3f-i). The altered domains can occur either within the interiors of the apatite crystals or along grain boundaries (Fig. 3f-h), and may locally contain monazite-(Ce) inclusions or interstitial fine-grained monazite-(Ce) (Fig. 3g-i).

Monazite-(Ce)

Except for the fine-grained monazite-(Ce) associated with metasomatized apatite (Fig. 3g-i), most monazite-(Ce) grains are randomly distributed and occur interstitial to the carbonate minerals (Fig. 4). They display various crystal shapes and sizes. Some grains are euhedral and over 500 μm in length (Fig. 4a), but most grains are euhedral to subhedral and ~100 μm to < 500 μm in length (Fig. 4b-c). Locally, monazite-(Ce) grains are anhedral and fine-grained (< 20 μm), forming aggregate veinlets (Fig. 4d). Most of the grains show erosional and porous textures under BSE images (Fig. 5) and can display various zoning in BSE images, including no obvious zonation (Fig. 5a), oscillatory to sector zonings (Fig. 5b-c), or patchy zonings with irregular dark and light domains (Fig.

5d-f). These were the grains analyzed in this study. No analyses were made on the monazite-(Ce) inclusions or fine grains associated with the altered apatite.

Results

Monazite-(Ce) U-Th-Pb dating

The results from monazite-(Ce) U-Th-Pb dating are listed in Supplementary Table 1. Monazite-(Ce) grains from a carbonated syenite sample (16MY-25) have relatively high U (44-928 ppm) and Th concentrations, and hence yield both U-Pb and Th-Pb ages. They have consistent and narrow ranges of $^{238}U/^{206}Pb$ and $^{232}Th/^{208}Pb$ ages with weighted mean values of 237±7 Ma (N=18) and 231±3 Ma (N=19), respectively (Fig. 6a-c). In contrast, monazite-(Ce) grains from other samples are commonly Th-rich and U-poor. Therefore, most LA-ICP-MS and SHRIMP spot analyses yield discordant and imprecise U-Pb ages, but high-quality Th-Pb ages. Weighted mean $^{232}Th/^{208}Pb$ ages are hence adopted for these samples. Overall, spot analyses of monazite-(Ce) grains from both complexes (also including those from sample 16MY-25) show a large range of Th-Pb ages from ~210 Ma to ~410 Ma, but have an obvious age peak at ~230 Ma and a subordinate peak at ~240 to ~250 Ma in the histogram (Fig. 7). The relatively old ages (most from ~260 to ~410 Ma) were obtained from the dark domains of monazite-(Ce) grains with patchy zoning (Fig. 5d-f). The influence of common Pb on these older ages can be precluded because all the analyses contain negligible common Pb contents, and there are no differences for common Pb signals between older and younger monazite-(Ce) grains. Excluding the

296 sporadic older data (Fig. 7), three samples have similar weighted mean Th-Pb ages of
297 229±3 Ma (N=19; sample 16MY-46:), 226±2 Ma (N=20; sample 14MY-25), and 229±2
298 Ma (N=54; sample SXD-26) (Fig. 6d-f). These Th-Pb ages are also consistent with the
299 U-Pb age from sample 16MY-25. However, sample 16MY-33 has an older weighted
300 mean LA-ICP-MS Th-Pb age of 253±7 Ma (N=14; Fig. 8a) compared to the other
301 samples. This age is indistinguishable from a weighted mean Th-Pb age of 248±10 Ma
302 (N=15) analyzed by SHRIMP II (Fig. 8b) for the same samples.

303 **Trace elements of apatite**

304 The dataset of trace elements of apatite is listed in Supplementary Table 2. Apatite
305 grains from the Miaoya and Shaxiongdong complexes contain high but variable (REE+Y)
306 concentrations. Primary apatite grains in the Miaoya complex display similar steep
307 right-sloping, chondrite-normalized REE patterns (Fig. 9a-b). Under CL imaging, the
308 green cores of the primary apatite have REE contents varying from 7883 to 9989 ppm,
309 which are slightly lower than those of rims of blue or purple domains (8411 to 16076
310 ppm). Primary apatite grains in the Shaxiongdong complex, however, show two types of
311 chondrite-normalized REE patterns. The primary CL green apatite displays steep
312 right-sloping REE patterns and relative low REE concentrations (6869 to 14715 ppm);
313 whereas the CL purple domains and grains have higher REE contents of 17825 to 29113
314 ppm and show nearly flat patterns from La to Nd patterns but steep right-inclined profiles
315 from Sm to Lu (Fig. 9c-d). Compared to the primary apatite, the altered apatite grains

316 have lower REE concentrations and show various REE patterns in both the Miaoya and
317 Shaxiongdong complexes. The altered apatite grains from the Miaoya complex show
318 right-sloping, chondrite-normalized REE patterns but with slightly gentle slope from La
319 to Eu compared to the primary domains (Fig 9a-b), whereas those in the Shaxiongdong
320 complex display nearly flat or slightly left-inclined profiles from La to Eu but
321 right-inclined profiles from Gd to Lu (Fig. 9c-d). There are no significant Eu or Ce
322 anomalies in chondrite-normalized REE patterns for both primary and altered apatite.

323 **Nd isotopes**

324 The results of Nd isotope analyses are listed in Supplementary Table 3. In the Miaoya
325 complex, primary apatite grains have $^{147}Sm/^{144}Nd$ and $^{143}Nd/^{144}Nd$ ratios varying from
326 0.07446 to 0.10219 and 0.512383 to 0.512472, respectively. In comparison, primary
327 apatite grains in the Shaxiongdong complex have slightly higher $^{147}Sm/^{144}Nd$ ratios of
328 0.09028 to 0.17573 and $^{143}Nd/^{144}Nd$ ratios of 0.512522 to 0.512784. We also attempted to
329 obtain the Nd isotopes from the altered apatite domains. However, the relatively large
330 laser spots (60 or 90 μm) have exceeded some narrow altered domains, and hence the
331 analyzed results may incorporate variable proportions of the primary domains. Compared
332 to primary apatite, the altered domains have relatively higher $^{147}Sm/^{144}Nd$ ratios but
333 similar $^{143}Nd/^{144}Nd$ ratios for both complexes. They have $^{147}Sm/^{144}Nd$ ratios of 0.08912
334 to 0.12028 and $^{143}Nd/^{144}Nd$ ratios of 0.512418 to 0.512492 for the Miaoya complex, and

335 $^{147}Sm/^{144}Nd$ ratios of 0.09714 to 0.20779 and $^{143}Nd/^{144}Nd$ ratios of 0.512534 to 0.512791
336 for Shaxiongdong complex.

337 Compared to apatite, monazite-(Ce) grains from both the Miaoya and Shaxiongdong
338 complexes have relatively uniform but slightly lower Nd isotopic compositions and there
339 are no obvious differences in Sm-Nd isotopes for monazite-(Ce) grains with different
340 zonings. Monazite-(Ce) in the Miaoya complex has $^{147}Sm/^{144}Nd$ and $^{143}Nd/^{144}Nd$ ratios
341 varying from 0.06578 to 0.09564 and from 0.512385 to 0.512465, respectively. In the
342 Shaxiongdong complex, $^{147}Sm/^{144}Nd$ and $^{143}Nd/^{144}Nd$ ratios of monazite-(Ce) vary from
343 0.05965 to 0.07632 and from 0.512479 to 0.512558, respectively.

344 **Discussion**

345 **Two possible interpretations for monazite-(Ce) ages**

346 Both the Miaoya and Shaxiongdong carbonatite-alkaline complexes have been
347 confirmed to have formed at ~430-440 Ma by zircon U-Th-Pb ages (Fig. 10) (Xu et al.
348 2008; Ying et al. 2017; Zhu et al. 2017; Chen et al. 2018; Su et al. 2019). However,
349 monazite-(Ce) Th-Pb ages obtained from both complexes are significantly younger than
350 zircon U-Th-Pb ages. All the spot analyses have an age peak at ~230 Ma and a sub-peak
351 at ~240 to 250 Ma in the histogram (Fig. 7), and different samples have weighted Th-Pb
352 ages from 230 Ma to 250 Ma (Fig. 6, 8). These ages are roughly the same as a
353 monazite-(Ce) age of ~230 to 245 Ma, columbite U-Pb age of 233 Ma, and bastnäsite-(Ce)
354 age of ~210 Ma for the Miaoya carbonatite that have been reported in previous studies

(Xu et al. 2014; Ying et al. 2017; Zhang et al. 2019) (Fig. 10). They are synchronous with the regional metamorphism during the closure of the Mianlue Ocean (210-250 Ma; Wu and Zheng, 2013), which resulted in the final collision of the North China Craton and Yangtze Block. Therefore, these monazite-(Ce) ages appear to correspond to the regional metamorphic overprint on the Silurian carbonatite-alkaline complexes.

There are two possible explanations for the formation of younger monazite-(Ce): (1) Formation of monazite-(Ce) grains during post-emplacement metamorphism possibly related to the alteration of apatite; and (2) partial to complete modification of Silurian primary monazite-(Ce). These two processes represent different enrichment histories for REE in carbonatite-alkaline related REE deposits. The first model indicates that REE remobilization may be significant during post-magmatism events and could be responsible for REE enrichment in carbonatite-related REE deposits. In contrast, the second model suggests that magmatic-hydrothermal evolution of carbonatite intrusions can result in economic REE enrichment but may undergo a late stage metamorphic overprint.

Formation of Triassic monazite-(Ce) related to metasomatic alteration of apatite

Apatite with high total REE concentrations is a common phosphate mineral in carbonatites from the Miaoya and Shaxiongdong complex. These apatite grains can be locally enveloped in carbonate or silicate minerals (Fig. 3a), suggesting that primary apatite is one of the earliest minerals to crystallize out from the carbonatite magma. Some

375 apatite grains have cores with relative lower REE contents compared to rims (Fig. 9). The
376 above textural and geochemical characteristics of Type I apatite from the carbonatites are
377 similar to Type I igneous apatite summarized by Chakhmouradian et al. (2017). The
378 compositional evolution of the apatite likely resulted from the fractionation of carbonate
379 and silicate minerals in the carbonatite magma. Therefore, Type II apatite grains with
380 homogeneous textures and higher REE contents likely appeared relatively late during the
381 crystallization of the magma.

382 However, these apatite grains were metasomatized by hydrothermal fluids during the
383 Triassic. The altered apatite grains from the Miaoya and Shaxiongdong complexes show
384 typical replacement textures under BSE imaging, which are similar to apatites resulting
385 from fluid metasomatism widely reported in carbonatite and hydrothermal ore systems (e.
386 g., IOCG and IOA deposit; Smith et al. 1999; Stosch et al. 2011; Li and Zhou, 2015;
387 Broom-Fendley et al. 2016, 2017; Zeng et al. 2016; Ren et al. 2019). The altered apatite
388 domains commonly contain monazite-(Ce) inclusions or are surrounded by fined-grained
389 monazite-(Ce) (Fig. 3), and have REE concentrations lower than the primary apatite (Fig.
390 9). Such textural and geochemical characteristics suggest that the REE were leached out
391 of the primary apatite as monazite-(Ce) during the Triassic metasomatic event.

392 The formation of monazite from metasomatic alteration of apatite has been well
393 confirmed by experimental studies (e.g., Harlov et al. 2003, 2005, 2015; Budzyń et al.
394 2011). Besides, it has been widely accepted that fluids enriched in anionic ligands are

beneficial for the mobilization of REE through hydrothermal processes (e.g., Cl and F; Harlov et al. 2005; Li and Zhou, 2015; Williams-Jones et al. 2012; Song et al. 2015). This scenario is also suitable for the Miaoya and Shaxiongdong complexes. Our studies show that such fluids are more efficient at removing LREE rather than HREE during metasomatic alteration of the apatite, and hence plot with a gentle REE chondrite-normalized slope in the altered domains (Fig. 9). REE remobilization similar to this has been reported by Broom-Fendley et al. (2016, 2017) in natural carbonatites.

Resetting U-Th-Pb isotopes of the early Paleozoic monazite-(Ce)

Except for the fine-grained monazite-(Ce) associated with apatite alteration discussed above, most monazite-(Ce) grains in the Miaoya and Shaxiongdong carbonatites are not spatially associated with apatite and consist of much larger crystals (Fig. 4). There is no obvious textural evidence supporting a genetic link related to leaching of REE from apatite. In contrast, these monazite-(Ce) grains show porous textures and many have patchy zoning consisting of irregularly shaped dark and light domains in the BSE images, which are typical of metasomatic alteration via coupled dissolution-reprecipitation (Fig. 5). They have variable monazite-(Ce) ages (210-410 Ma; Fig. 7), suggesting that they likely record disturbed U-Th-Pb isotopic ages. Previous experimental work has confirmed that monazite-(Ce) can be metasomatically altered by alkali-bearing fluids, which also depletes the Pb content (Harlov et al. 2010, 2011). Similar total Pb loss and resetting of the U-Th-Pb system in monazite-(Ce) from metasomatic alteration have also

been reported in natural samples as well as in experimental systems (e.g., Williams et al. 2011; Grand Homme et al. 2016; Weinberg et al. 2020). Thus, the large range of monazite-(Ce) ages from 210 to 410 Ma in the Shaxiongdong and Miaoya Complex can form by variable Pb loss during fluid metasomatism. Most grains have a peak age of ~230 Ma, indicating that metasomatic alteration of monazite-(Ce) is widespread and extensive during Triassic tectonothermal events. Relatively older ages (most from 260 to 410 Ma) were obtained from irregular dark domains of some monazite-(Ce) grains, and likely represent a variable but slightly weak Pb loss relative to the ~230 Ma grains. These ages are geologically meaningless variably reset Th-Pb ages. Zhang et al. (2019) reported a U-Pb age of 414±11 Ma for monazite-(Ce) from the Miaoya complex, which likely represents the least-altered sample. *In situ* Nd analyses of monazite-(Ce) with different zoning and ages show relatively uniform ratios, which are identical to the initial Nd ratios of primary apatite as well as whole rock (Fig. 11; Xu et al. 2008; Su et al.2019). Such isotopic features further confirm that all these grains were crystallized from the igneous complex and underwent metasomatism during late stage tectonothermal events.

Since both metasomatic alteration of primary monazite-(Ce) and new phases of monazite-(Ce) by remobilization of REE from altered apatite could have been formed in the Miaoya and Shaxiongdong carbonatites during the Triassic tectonothermal event, it is necessary to evaluate which processes are vital for the generation of the REE deposit. To address the above concerns, mass-balance calculations, based on mass proportions and

435 the REE contents of monazite-(Ce) and apatite, are adopted by this study to evaluate how
436 much monazite-(Ce) can be produced from metasomatic alteration of the apatite. We
437 assumed that the mineral volume proportion of the primary and the altered apatite can be
438 approximately represented by estimation from microscopic imaging. Using their
439 respective mineral densities [apatite: 3.18 g/cm^3; monazite-(Ce): 5.26 g/cm^3], the mass
440 proportions for the apatite and monazite-(Ce) were obtained. Based on our microscope
441 observations, the volumetric distribution of apatite and independent monazite-(Ce) in
442 samples vary from 0-20 vol.% and 0-1 vol.%, respectively. Then, assuming a volume
443 ratio of 95.2:4.8 for apatite to independent monazite-(Ce) based on their average
444 volumetric distributions (10 vol.% and 0.5 vol.%, respectively), a mass ratio of 92.4:7.6
445 for apatite to monazite-(Ce) was calculated. Here, based on our petrographical
446 observations, we assumed that less than 30% of apatite has been totally altered. A total
447 REE content of 579612 ppm for monazite-(Ce) (Ying et al. 2017), and the average REE
448 contents of primary apatite and altered apatite (Miaoya: 9662 and 4157 ppm;
449 Shaxiongdong: 15483 and 6940 ppm) were used for the modal calculation. The ideal
450 mass ratios of apatite to monazite-(Ce) resulting from metasomatic alteration of the
451 apatite was 99.7:0.3 in the Miaoya complex and 99.5:0.5 in the Shaxiongdong complex,
452 which are more than an order of magnitude higher than the mass ratios of apatite to
453 independent monazite-(Ce) (92.4:7.6) in our samples. However, the ideal mass ratios of
454 apatite to monazite-(Ce) formed by metasomatic alteration of the apatite are almost

consistent with the proportion of the altered apatite versus monazite-(Ce) inclusions and associated fine-grained monazite-(Ce) (Fig. 3g-i). This suggests that REE remobilization is most likely confined to the immediate vicinity of the altered apatite. In consideration of the fact that the proportions of monazite-(Ce) inclusions or fine-grained monazite-(Ce) associated with altered apatite are much less compared to that of the independent monazite-(Ce) grains, modal calculations suggest that most of monazite-(Ce) grains in this study were crystallized from the Silurian carbonatite, but underwent variable degrees of Pb loss during fluid-induced metasomatism, leading to a wide range in Th-Pb ages. Thus, we suggest that REE remobilization was not a key enrichment process in the Miaoya and Shaxiongdong complexes.

An integrated model for the Miaoya and Shaxiongdong complexes

In this study, we present detailed textural, and *in situ* elemental and isotopic data for monazite-(Ce) and apatite from the Miaoya and Shaxiongdong complexes from the South Qinling Belt, Central China. These data have enabled us to decipher a complicated REE enrichment and remobilization history. The carbonatite-alkaline complexes were emplaced at 440-430 Ma, and carbonatite melts formed from extensive fractionation carbonated alkaline magmas (Su et al. 2019). During the fractionation of the carbonatites, REE-bearing apatite and monazite-(Ce) crystallized through magma differentiation as the major primary host of REE in the carbonatite (Fig. 12a). However, the complexes

underwent metasomatic modification during the closure of the Mianlue Ocean in the Triassic. Apatite and monazite-(Ce)) were altered by metasomatic fluids. Monazite-(Ce) grains were partly or fully modified (Fig. 12b), resulting in a wide range of Th-Pb ages for monazite-(Ce). The apatite was leached of REEs, which resulted in fine-grained monazite-(Ce), which mostly occur as inclusions within the altered apatite domains or associated with the altered apatite as rim grains (Fig. 12b).

Implications for REE enrichment in carbonatites

Previous studies have shown that metasomatism can result in significant REE remobilization in many IOCG or IOA deposits where apatite is a common gangue mineral (e.g., Harlov et al. 2002; Li et al. 2015, 2018; Zeng et al. 2016; Palma et al. 2019). The metasomatic fluids leached LREE from the apatite, resulting in the crystallization of monazite, allanite, and bastnäsite. Such an REE remobilization event can transfer REE from the REE-bearing apatite to form monazite, which makes the deposit more economic. More studies have shown that metasomatism also occurs in REE phosphate minerals in carbonatite related systems too, such as the Bayan Obo deposit (Song et al. 2018), the Cummins Range carbonatite complex (Downes et al.2016), and the Gifford Creek carbonatite complex (Zi et al. 2017; Slezak and Spandler, 2019). Monazites from these carbonatites mostly record multiple episodes of U-Th-Pb ages, which can be protracted over hundreds of millions of years. For example, *in situ* monazite U-Th-Pb ages from 361 to 913 Ma for the Bayan Obo deposit are significantly younger than the initial ore

494 formation at ~1.3 Ga (Smith et al. 2015; Song et al. 2018; Yang et al. 2019). Monazite in
495 the Gifford Creek carbonatite complex yield U-Pb ages ranging from ca. 1250 Ma to 815
496 Ma, compared to a magmatic zircon U-Pb age of ~1370 Ma (Slezak and Spandler, 2019).

497 Our new dataset reveals that carbonatite-alkaline complexes in the South Qinling Belt
498 were initially formed at 440-430 Ma and underwent Triassic metasomatism. Based on our
499 observations, minerals have the capability to resist metasomatic alteration in carbonatite
500 systems in the following order zircon > apatite > monazite (Millonig et al. 2013; Slezak
501 and Spandler, 2019). Therefore, monazite U-Pb dating is more likely to record the timing
502 of the subsequent metasomatic event or mixed signatures between carbonatite
503 emplacement and a subsequent metasomatic event. In other words, most younger
504 monazite ages are due to the partial or complete resetting of primary U-Pb isotopic
505 signatures. Meanwhile, formation of monazite from apatite during metasomatic events
506 can also occur in carbonatites, but its role in the formation of economic REE ores can be
507 various and should be evaluated in different deposits. Thus, detailed textural observations
508 in combination with *in situ* elemental and isotopic data appear to be essential in
509 understanding the genesis of these REE deposits.

510 **Acknowledgments**

511 This study was financially supported the national key R&D program of China
512 (2017YFC0602401), NSFC Project (41822203; 41902087), and the Fundamental
513 Research Funds for the Central Universities, China University of Geosciences (Wuhan)

514 (CUG140618 and CUGCJ1711). We are grateful to Zu-Wei Lin, Wang Liao, Sheng-Ren
515 Chang and Li-Ping Zeng for their help in the field and lab works. We greatly appreciate
516 the constructive reviews by Sam Broom-Fendley and Martin Smith, and editorial
517 comments by Daniel Harlov. This is contribution 40 from CUG Center for Research in
518 Economic Geology and Exploration Targeting (CREGET).

519

520 **References**

521 Aleinikoff, J.N., Schenck, W.S., Plank, M.O., Srogi, L., Fanning, C.M., Kamo, S.L., and
522 Bosbyshell, H. (2006) Deciphering igneous and metamorphic events in high-grade
523 rocks of the Wilmington Complex, Delaware: Morphology, cathodoluminescence
524 and backscattered electron zoning, and SHRIMP U-Pb geochronology of zircon and
525 monazite. Geological Society of America Bulletin, 118, 39-64

526 Boynton, W.V. (1984) Cosmochemistry of the Rare Earth Elements: Meteorite Studies. In
527 P. Henderson, Ed. Developments in Geochemistry, 2, p. 63-114. Elsevier.

528 Broom-Fendley, S., Styles, M.T., Appleton, J.D., Gunn, G., and Wall, F. (2016) Evidence
529 for dissolution-reprecipitation of apatite and preferential LREE mobility in
530 carbonatite-derived late-stage hydrothermal processes. American Mineralogist, 101,
531 596-611.

532 Broom-Fendley, S., Brady, A.E., Wall, F., Gunn, G., and Dawes, W. (2017) REE minerals
533 at the Songwe Hill carbonatite, Malawi: HREE-enrichment in late-stage apatite. Ore
534 Geology Reviews, 81, 23-41.
535 Budzyń, B., Harlov, D.E., Williams, M.L., and Jercinovic, M.J. (2011) Experimental
536 determination of stability relations between monazite, fluorapatite, allanite, and
537 REE-epidote as a function of pressure, temperature, and fluid composition.
538 American Mineralogist, 96, 1547-1567.
539 Bühn, B. (2001) Rare-earth element systematics of carbonatitic fluorapatites, and their
540 significance for carbonatite magma evolution. Contributions to Mineralogy and
541 Petrology, 141, 572-591.
542 Catlos, E.J., Dubey, C.S., and Sivasubramanian, P. (2008) Monazite ages from
543 carbonatites and high-grade assemblages along the Kambam Fault (Southern
544 Granulite Terrane, South India). American Mineralogist, 93, 1230-1244.
545 Chakhmouradian, A.R., and Wall, F. (2012) Rare Earth Elements: Minerals, Mines,
546 Magnets (and More). Elements, 8, 333-340.
547 Chakhmouradian, A.R., Reguir, E.P., Zaitsev, A.N., Couëslan, C., Xu, C., Kynický, J.,
548 Mumin, A.H., and Yang, P. (2017) Apatite in carbonatitic rocks: Compositional
549 variation, zoning, element partitioning and petrogenetic significance. Lithos,
550 274-275, 188-213.

551 Chen, W., Honghui, H., Bai, T., and Jiang, S. (2017) Geochemistry of monazite within
552 carbonatite related REE deposits. Resources, 6, 51.
553 Chen, W., Lu, J., Jiang, S., Ying, Y., and Liu, Y. (2018) Radiogenic Pb reservoir
554 contributes to the rare earth element (REE) enrichment in South Qinling carbonatites.
555 Chemical Geology, 494, 80-95.
556 Dong, Y., and Santosh, M. (2016) Tectonic architecture and multiple orogeny of the
557 Qinling Orogenic Belt, Central China. Gondwana Research, 29, 1-40.
558 Downes, P.J., Dunkley, D.J., Fletcher, I.R., McNaughton, N.J., Rasmussen, B., Jaques,
559 A.L., Verrall, M., and Sweetapple, M.T. (2016) Zirconolite, zircon and monazite-(Ce)
560 U-Th-Pb age constraints on the emplacement, deformation and alteration history of
561 the Cummins Range Carbonatite Complex, Halls Creek Orogen, Kimberley region,
562 Western Australia. Mineralogy and Petrology, 110, 199-222.
563 Engi, M. (2017) Petrochronology Based on REE-Minerals: Monazite, Allanite, Xenotime,
564 Apatite. Reviews in Mineralogy and Geochemistry, 83, 365-418.
565 Fletcher, I.R., McNaughton, N.J., Davis, W.J., and Rasmussen, B. (2010) Matrix effects
566 and calibration limitations in ion probe U-Pb and Th-Pb dating of monazite.
567 Chemical Geology, 270, 31-44.
568 Gao, S., Zhang, B., Gu, X., Xie, Q., Gao, C., and Guo, X. (1995) Silurian-Devonian
569 provenance changes of South Qinling Basins: Implications for accretion of the
570 Yangtze (South China) to the North China cratons. Tectonophysics, 250, 183-197.

571 Gittins, J. (1989) The origin and evolution of carbonatite magmas. In Bell, K., Eds.,
572 Carbonatites: genesis and evolution, p. 580-600. The Academic Division of Unwin
573 Hyman Ltd, London.
574 Goodenough, K.M., Wall, F., and Merriman, D. (2017) The rare earth elements: Demand,
575 global resources, and challenges for resourcing future generations. Natural
576 Resources Research, 27, 201-216.
577 Grand Homme, A., Janots, E., Seydoux-Guillaume, A., Guillaume, D., Bosse, V., and
578 Magnin, V. (2016) Partial resetting of the U-Th-Pb systems in experimentally altered
579 monazite: Nanoscale evidence of incomplete replacement. Geology, 44, 431-434.
580 Harlov, D.E., Andersson, U.B., Förster, H., Nyström, J.O., Dulski, P., and Broman, C.
581 (2002) Apatite-monazite relations in the Kiirunavaara magnetite-apatite ore,
582 Northern Sweden. Chemical Geology, 191, 47-72.
583 Harlov, D.E., and Förster, H. (2003) Fluid-induced nucleation of (Y+REE)-phosphate
584 minerals within apatite: Nature and experiment. Part II. Fluorapatite. American
585 Mineralogist, 88, 1209-1229.
586 Harlov, D.E., Wirth, R., and Förster, H. (2005) An experimental study of
587 dissolution-reprecipitation in fluorapatite: Fluid infiltration and the formation of
588 monazite. Contributions to Mineralogy and Petrology, 150, 268-286.

589 Harlov, D.E., and Hetherington, C.J. (2010) Partial high-grade alteration of monazite
590 using alkali-bearing fluids: Experiment and nature. American Mineralogist, 95,
591 1105-1108.
592 Harlov, D.E., Wirth, R., and Hetherington, C.J. (2011) Fluid-mediated partial alteration in
593 monazite: The role of coupled dissolution-reprecipitation in element redistribution
594 and mass transfer. Contributions to Mineralogy and Petrology, 162, 329-348.
595 Harlov, D.E. (2015) Apatite: A fingerprint for metasomatic processes. Elements, 11,
596 171-176.
597 Hu, Z., Zhang, W., Liu, Y., Gao, S., Li, M., Zong, K., Chen, H., and Hu, S. (2015)
598 “Wave” signal-smoothing and mercury-removing device for laser ablation
599 quadrupole and multiple collector ICPMS analysis: Application to lead isotope
600 analysis. Analytical Chemistry, 87, 1152-1157.
601 Kim, N., Cheong, A.C., Yi, K., Jeong, Y., and Koh, S.M. (2016) Post-collisional
602 carbonatite-hosted rare earth element mineralization in the Hongcheon area, central
603 Gyeonggi massif, Korea: Ion microprobe monazite U-Th-Pb geochronology and
604 Nd-Sr isotope geochemistry. Ore Geology Reviews, 79, 78-87.
605 Le Bas, M.J., and Handley, C.D. (1979) Variation in apatite composition in ijolitic and
606 carbonatitic igneous rocks. Nature, 279, 54-56.
607 Li, S. (1980) Geochemical features and petrogenesis of Miaoya carbonatites, Hubei
608 Province. Geochimica, p. 345-355 (in Chinese).

609 Li, S. (1991) Geochemistry and petrogenesis of the Shaxiongdong carbonatite complex,
610 Hubei Province. Geochimica, 245-254 (in Chinese).
611 Li, X., and Zhou, M. (2015) Multiple stages of hydrothermal REE remobilization
612 recorded in fluorapatite in the Paleoproterozoic Yinachang Fe-Cu-(REE) deposit,
613 Southwest China. Geochimica Et Cosmochimica Acta, 166, 53-73.
614 Li, X., Zhou, M., Yang, Y., Zhao, X., and Gao, J. (2018) Disturbance of the Sm-Nd
615 isotopic system by metasomatic alteration: A case study of fluorapatite from the Sin
616 Quyen Cu-LREE-Au deposit, Vietnam. American Mineralogist, 103, 1487-1496.
617 Ling, M., Liu, Y., Williams, I.S., Teng, F., Yang, X., Ding, X., Wei, G., Xie, L., Deng, W.,
618 and Sun, W. (2013) Formation of the world's largest REE deposit through protracted
619 fluxing of carbonatite by subduction-derived fluids. Scientific Reports, 3.
620 Liu, Y., Hu, Z., Gao, S., Günther, D., Xu, J., Gao, C., and Chen, H. (2008) In situ analysis
621 of major and trace elements of anhydrous minerals by LA-ICP-MS without applying
622 an internal standard. Chemical Geology, 257, 34-43.
623 Liu, Y., Gao, S., Hu, Z., Gao, C., Zong, K., and Wang, D. (2010) Continental and oceanic
624 crust recycling-induced melt-peridotite interactions in the Trans-North China
625 Orogen: U-Pb dating, Hf isotopes and trace elements in zircons from mantle
626 xenoliths. Journal of Petrology, 51, 537-571.
627 Ludwig, K.R. (2003) ISOPLOT 3.00: A geochronological toolkit for Microsoft Excel.
628 Berkeley Geochronology Center Special Publication, 1-70.

629 Ludwig, K.R. (2009) Squid 2.50. A User's Manual: Berkeley, California, Berkeley
630 Geochronology Centre Special Publication, 95.
631 Mao, M., Rukhlov, A.S., Rowins, S.M., Spence, J., and Coogan, L.A. (2016) Apatite trace
632 element compositions: A robust new tool for mineral exploration. Economic
633 Geology, 111, 1187-1222.
634 Mattauer, M., Matte, P., Malavieille, J., Tapponnier, P., Maluski, H., Qin, X.Z., Lun, L.Y.,
635 and Qin, T.Y. (1985) Tectonics of the Qinling belt: Build-up and evolution of eastern
636 Asia. Nature, 317, 496.
637 Millonig, L.J., Gerdes, A., and Groat, L.A. (2012) U-Th-Pb geochronology of
638 meta-carbonatites and meta-alkaline rocks in the southern Canadian Cordillera: A
639 geodynamic perspective. Lithos, 152, 202-217.
640 Millonig, L.J., Gerdes, A., and Groat, L.A. (2013) The effect of amphibolite facies
641 metamorphism on the U-Th-Pb geochronology of accessory minerals from
642 meta-carbonatites and associated meta-alkaline rocks. Chemical Geology, 353,
643 199-209.
644 Palma, G., Barra, F., Reich, M., Valencia, V., Simon, A.C., Vervoort, J., Leisen, M., and
645 Romero, R. (2019) Halogens, trace element concentrations, and Sr-Nd isotopes in
646 apatite from iron oxide-apatite (IOA) deposits in the Chilean iron belt: Evidence for
647 magmatic and hydrothermal stages of mineralization. Geochimica Et Cosmochimica
648 Acta, 246, 515-540.

649 Poletti, J.E., Cottle, J.M., Hagen-Peter, G.A., and Lackey, J.S. (2016) Petrochronological
650 constraints on the origin of the Mountain Pass ultrapotassic and carbonatite intrusive
651 suite, california. Journal of Petrology, 8, 1555-1598.
652 Putnis, A. (2002) Mineral replacement reactions: From macroscopic observations to
653 microscopic mechanisms. Mineralogical Magazine, 66, 689-708.
654 Putnis, A. (2009) Mineral replacement reactions. Reviews in Mineralogy and
655 Geochemistry, 70, 87-124.
656 Ratschbacher, L., Hacker, B.R., Calvert, A., Webb, L.E., Grimmer, J.C., McWilliams,
657 M.O., Ireland, T., Dong, S., and Hu, J. (2003) Tectonics of the Qinling (Central
658 China): Tectonostratigraphy, geochronology, and deformation history.
659 Tectonophysics, 366, 1-53.
660 Ren, Y., Yang, X., Wang, S., and Öztürk, H. (2019) Mineralogical and geochemical study
661 of apatite and dolomite from the Bayan Obo giant Fe-REE-Nb deposit in Inner
662 Mongolia: New evidences for genesis. Ore Geology Reviews, 109, 381-406.
663 Simandl, G.J., and Paradis, S. (2018) Carbonatites: Related ore deposits, resources,
664 footprint, and exploration methods. Applied Earth Science, 127, 123-152.
665 Slezak, P., and Spandler, C. (2019) Carbonatites as recorders of mantle-derived
666 magmatism and subsequent tectonic events: An example of the Gifford Creek
667 Carbonatite Complex, Western Australia. Lithos, 328-329, 212-227.

668 Smith, M.P., Henderson, P., and Peishan, Z. (1999) Reaction relationships in the Bayan
669 Obo Fe-REE-Nb deposit Inner Mongolia, China: Implications for the relative
670 stability of rare-earth element phosphates and fluorocarbonates. Contributions to
671 Mineralogy and Petrology, 134, 294-310.
672 Smith, M.P., Campbell, L.S., and Kynicky, J. (2015) A review of the genesis of the world
673 class Bayan Obo Fe–REE–Nb deposits, Inner Mongolia, China: Multistage
674 processes and outstanding questions. Ore Geology Reviews, 64, 459-476.
675 Song, W., Xu, C., Veksler, I.V., and Kynicky, J. (2015) Experimental study of REE, Ba,
676 Sr, Mo and W partitioning between carbonatitic melt and aqueous fluid with
677 implications for rare metal mineralization. Contributions to Mineralogy and
678 Petrology, 171, 1-12.
679 Song, W., Xu, C., Smith, M.P., Chakhmouradian, A.R., Brenna, M., Kynický, J., Chen,
680 W., Yang, Y., Deng, M., and Tang, H. (2018) Genesis of the world's largest rare earth
681 element deposit, Bayan Obo, China: Protracted mineralization evolution over ~1 b.y.
682 Geology, 46, 323-326.
683 Spandler, C., Hammerli, J., Sha, P., Hilbert-Wolf, H., Hu, Y., Roberts, E., and Schmitz, M.
684 (2016) MKED1: A new titanite standard for in situ analysis of Sm-Nd isotopes and
685 U-Pb geochronology. Chemical Geology, 425, 110-126.

686 Stosch, H., Romer, R.L., Daliran, F., and Rhede, D. (2011) Uranium-lead ages of apatite
687 from iron oxide ores of the Bafq District, East-Central Iran. Mineralium Deposita,
688 46, 9-21.
689 Su, J., Zhao, X., Li, X., Hu, W., Chen, M., and Xiong, Y. (2019) Geological and
690 geochemical characteristics of the Miaoya syenite-carbonatite complex, Central
691 China: Implications for the origin of REE-Nb-enriched carbonatite. Ore Geology
692 Reviews, 113, 103101.
693 Verplanck, P.L., Mariano, A.N., and Mariano, A. (2016) Rare earth ore geology of
694 carbonatites. In P.L. Verplanck, and M.W. Hitzman, Eds., Rare Earth and Critical
695 Elements in Ore Deposits, p. 5-32. Society of Economic Geologist, Littleton.
696 Wang, K., Wang, Z., Zhang, Y., and Wang, G. (2015) Geochronology and geochemistry of
697 mafic rocks in the Xuhe, Shaanxi, china: implications for petrogenesis and mantle
698 dynamics. Acta Geologica Sinica (English Edition), 89, 187-202.
699 Wang, L., Marks, M.A.W., Wenzel, T., Von Der Handt, A., Keller, J., Teiber, H., and
700 Markl, G. (2014) Apatites from the Kaiserstuhl Volcanic Complex, Germany: New
701 constraints on the relationship between carbonatite and associated silicate rocks.
702 European Journal of Mineralogy, 26, 397-414.
703 Wang, R., Xu, Z., Santosh, M., Liang, F., and Fu, X. (2017) Petrogenesis and tectonic
704 implications of the Early Paleozoic intermediate and mafic intrusions in the South

Qinling Belt, Central China: Constraints from geochemistry, zircon U-Pb geochronology and Hf isotopes. Tectonophysics, 712-713, 270-288.

Weinberg, R.F., Wolfram, L.C., Nebel, O., Hasalová, P., Závada, P., Kylander-Clark, A.R.C., and Becchio, R. (2020) Decoupled U-Pb date and chemical zonation of monazite in migmatites: The case for disturbance of isotopic systematics by coupled dissolution-reprecipitation. Geochimica Et Cosmochimica Acta, 269, 398-412.

Weng, Z., Jowitt, S.M., Mudd, G.M., and Haque, N. (2015) A detailed assessment of global rare earth element resources: Opportunities and challenges. Economic Geology, 110, 1925-1952.

Williams, M.L., Jercinovic, M.J., Harlov, D.E., Budzyń, B., and Hetherington, C.J. (2011) Resetting monazite ages during fluid-related alteration. Chemical Geology, 283, 218-225.

Williams-Jones, A.E., Migdisov, A.A., and Samson, I.M. (2012) Hydrothermal mobilisation of the rare earth elements - a tale of "ceria" and "yttria". Elements, 8, 355-360.

Wu, Y., and Zheng, Y. (2013) Tectonic evolution of a composite collision orogen: An overview on the Qinling-Tongbai-Hong'an-Dabie-Sulu Orogenic Belt in Central China. Gondwana Research, 23, 1402-1428.

723 Xu, C., Campbell, I.H., Allen, C.M., Chen, Y., Huang, Z., Qi, L., Zhang, G., and Yan, Z.
724 (2008) U-Pb zircon age, geochemical and isotopic characteristics of carbonatite and
725 syenite complexes from the Shaxiongdong, China. Lithos, 105, 118-128.
726 Xu, C., Chakhmouradian, A.R., Taylor, R.N., Kynicky, J., Li, W., Song, W., and Fletcher,
727 I.R. (2014) Origin of carbonatites in the South Qinling Orogen: Implications for
728 crustal recycling and timing of collision between the South and North China Blocks.
729 Geochimica Et Cosmochimica Acta, 143, 189-206.
730 Xu, L., Hu, Z., Zhang, W., Yang, L., Liu, Y., Gao, S., Luo, T., and Hu, S. (2015) In situ
731 Nd isotope analyses in geological materials with signal enhancement and non-linear
732 mass dependent fractionation reduction using laser ablation MC-ICP-MS. Journal of
733 Analytical Atomic Spectrometry, 30, 232-244.
734 Yang, K., Fan, H., Pirajno, F., and Li, X. (2019) The Bayan Obo (China) giant REE
735 accumulation conundrum elucidated by intense magmatic differentiation of
736 carbonatite. Geology, 47, 1198-1202.
737 Ying, Y., Chen, W., Lu, J., Jiang, S., and Yang, Y. (2017) In situ U-Th-Pb ages of the
738 Miaoya carbonatite complex in the South Qinling Orogenic Belt, central China.
739 Lithos, 290-291, 159-171.
740 Zeng, L., Zhao, X., Li, X., Hu, H., and McFarlane, C. (2016) In situ elemental and
741 isotopic analysis of fluorapatite from the Taocun magnetite-apatite deposit, Eastern
742 China: Constraints on fluid metasomatism. American mineralogist, 101, 2468-2483.

743 Zhang, C., Gao, S., Yuan, H., Zhang, G., Yan, Y., Luo, J., and Luo, J. (2007) Sr-Nd-Pb
744 isotopes of the Early Paleozoic mafic-ultramafic dykes and basalts from South
745 Qinling belt and their implications for mantle composition. Science in China Series
746 D: Earth Sciences, 50, 1293-1301 (in Chinese).
747 Zhang, W., Chen, W.T., Gao, J., Chen, H., and Li, J. (2019) Two episodes of REE
748 mineralization in the Qinling Orogenic Belt, Central China: In-situ U-Th-Pb dating
749 of bastnäsite and monazite. Mineralium Deposita, 54, 1265-1280.
750 Zhou, B., Li, Z., and Chen, C. (2017) Global potential of rare earth resources and rare
751 earth demand from clean technologies. Minerals, 7, 203.
752 Zhu, J., Wang, L., Peng, S., Peng, L., Wu, C., and Qiu, X. (2017) U-Pb zircon age,
753 geochemical and isotopic characteristics of the Miaoya syenite and carbonatite
754 complex, Central China. Geological Journal, 52, 938-954.
755 Zi, J., Gregory, C.J., Rasmussen, B., Sheppard, S., and Muhling, J.R. (2017) Using
756 monazite geochronology to test the plume model for carbonatites: The example of
757 Gifford Creek Carbonatite Complex, Australia. Chemical Geology, 463, 50-60.
758 Zong, K., Klemd, R., Yuan, Y., He, Z., Guo, J., Shi, X., Liu, Y., Hu, Z., and Zhang, Z.
759 (2017) The assembly of Rodinia: The correlation of early Neoproterozoic (ca. 900
760 Ma) high-grade metamorphism and continental arc formation in the southern
761 Beishan Orogen, southern Central Asian Orogenic Belt (CAOB). Precambrian
762 Research, 290, 32-48.

763

764 **Figure captions**

765 **Figure 1.** (a) Simplified geotectonic maps showing the geology of the South Qinling; (b)
766 a simplified map of the Miaoya syenite-carbonatite complex; (c) a simplified map of the
767 Shaxiongdong pyroxenite-syenite-carbonatite complex. S-NCC=the southern margin of
768 the North China Craton; N-YB=the northern margin of Yangtze Block.

769 **Figure 2.** Photographs of typical rocks and their field relationships in the Miaoya and
770 Shaxiongdong complexes. (a) Sharp contact between syenite and carbonatite in the
771 Miaoya complex; (b)-(c) Fresh calcite carbonatites with banded biotite (Bt) in the Miaoya
772 complex; (d) Ankerite carbonatite dyke cutting calcite carbonatites in the Miaoya
773 complex; (e)-(f) Carbonatite can occur as veins, mass, or microscopic aggregations of
774 calcite (see arrows) in pyroxenite and syenite from the Shaxiongdong complex; (g)
775 Biotite (Bt) together with aegirine (Aeg) is unevenly distributed through the rocks and
776 locally shows banded structures or massive appearance in carbonatite dykes.

777 **Figure 3.** Images showing typical apatite grains from the Miaoya and Shaxiongdong
778 complex. (a) photomicrographs (CPL: crossed-polarized light) showing relationships
779 between apatite and carbonate and silicate minerals; (b)-(c) CL and BSE images of
780 primary apatite grains with core-rim texture from the Miaoya complex; (d) CL images of
781 primary apatite grains from the Shaxiongdong complex; (e) CL image of homogeneous
782 primary apatite grains from the Miaoya complex; (f) alteration domains in apatites are
783 denoted by a greenish color under CL imaging; (g)-(i) BSE imaging of metasomatized

784 dark domains in apatite, occurring either in the interior of the apatite grain or along grain
785 boundaries. Monazite-(Ce) grains sometimes occur as inclusions within metasomatized
786 domains and veinlets surrounding the metasomatized apatite grains. Ap=apatite;
787 Bt=biotite; Cal=calcite; Kf= K-feldspar; Mnz=monazite-(Ce).

788 **Figure 4.** BSE images showing typically textural relationships of monazite-(Ce) from the
789 Miaoya and Shaxiongdong complexes. (a) Coarse-grained monazite-(Ce) grains
790 surrounded by calcite in a calcite carbonatite; (b)-(c) Medium to fine-grained independent
791 monazite-(Ce) or aggregates in calcite carbonatite; (d) Fine-grained monazite aggregate
792 veinlets in calcite carbonatite.

793 **Figure 5.** BSE images of representative monazite-(Ce) grains analyzed in this study.
794 Ages of spot LA-ICP-MS analyses are indicated.

795 **Figure 6.** (a) Concordia plot of monazite-(Ce) U-Pb ages and (b-f) weighted mean Th-Pb
796 age of monazite-(Ce) by LA-ICP-MS from the Miaoya (MY) and Shaxiongdong (SXD)
797 complex.

798 **Figure 7.** Histogram of monazite-(Ce) spot Th-Pb ages from the Miaoya (a) and
799 Shaxiongdong (b) complexes.

800 **Figure 8.** Weighted mean Th-Pb age of monazite-(Ce) by LA-ICP-MS (a) and SHRIMP
801 II (b) from the sample 16MY-33 in the Miaoya complex.

802 **Figure 9.** Chondrite-normalized REE patterns for primary and altered apatite. (a)-(b)
803 Primary apatite from the Miaoya complex displays steep right-sloping REE patterns, note

804 the different patterns between primary and altered grains; (c)-(d) Apatite grains from the
805 Shaxiongdong complex show variable REE patterns, the primary domains of green CL
806 display steep right-sloping REE patterns whereas the purple/blue CL domains and/or
807 grains show nearly flat patterns from La to Nd patterns but steep right-inclined profiles
808 from Sm to Lu. Note the green domains also have relative low REE contents compared to
809 purple/blue domains, and the altered domains commonly have lower LREE relative to
810 primary apatite. Normalization values are from Boynton (1984).

811 **Figure 10.** Summary of geochronological data from the Miaoya and Shaxiongdong
812 complex. Age data are compiled from this study, Li (1991; 1980), Xu et al. (2008), Ying
813 et al. (2017), Zhu et al. (2016), Chen et al. (2018), Su et al. (2019), and Zhang et al.
814 (2019).

815 **Figure 11.** Histograms showing εNd (t) values of monazite-(Ce) and apatite from the
816 Miaoya and Shaxiongdong complexes. The black dashed line is the average εNd (t) value
817 of whole rock from Xu et al. (2008) and Su et al. (2019). All εNd (t) values were
818 calculated using the U-Pb zircon age (440 Ma) obtained by Xu et al. (2008) and Su et al.
819 (2019).

820 **Figure 12.** Cartoons illustrating carbonatite formation and the REE remobilization
821 histories from the Miaoya and Shaxiongdong complex. (a) Crystallization of primary
822 apatite and monazite-(Ce) in the carbonatite-alkaline complex emplaced in the Early
823 Silurian; (b) The Triassic metasomatism event are responsible for the alteration of the
824 monazite-(Ce) and apatite.

This is the peer-reviewed, final accepted version for American Mineralogist, published by the Mineralogical Society of America.
The published version is subject to change. Cite as Authors (Year) Title. American Mineralogist, in press.
DOI: https://doi.org/10.2138/am-2021-7746. http://www.minsocam.org/

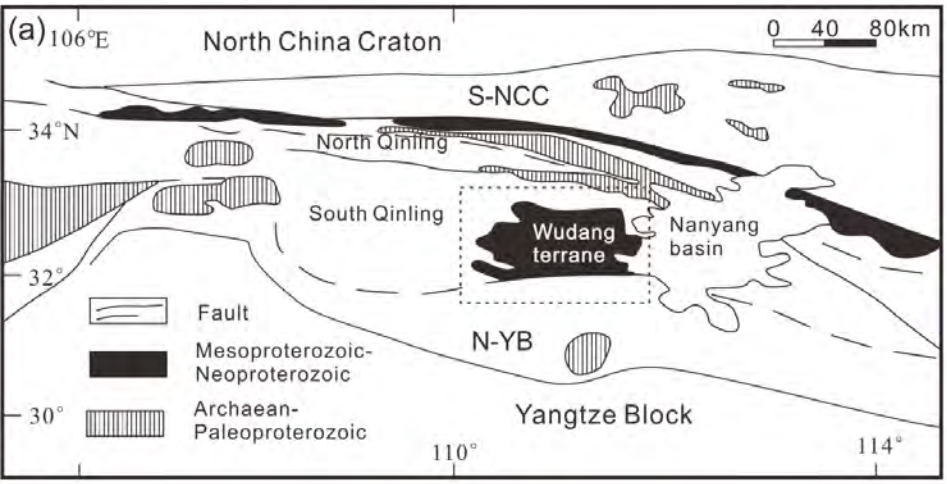

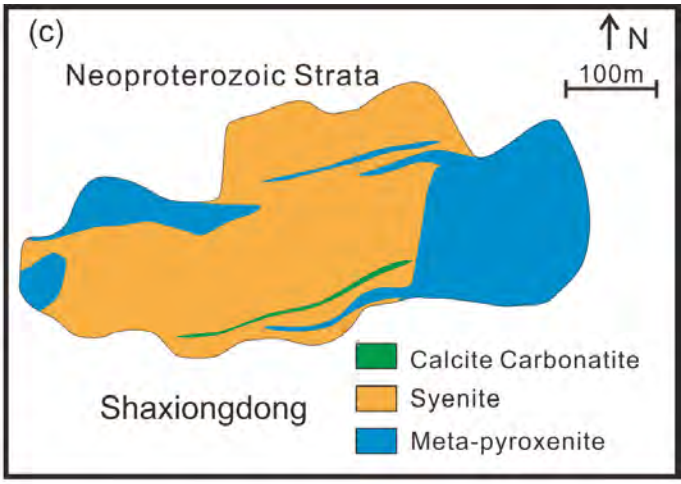

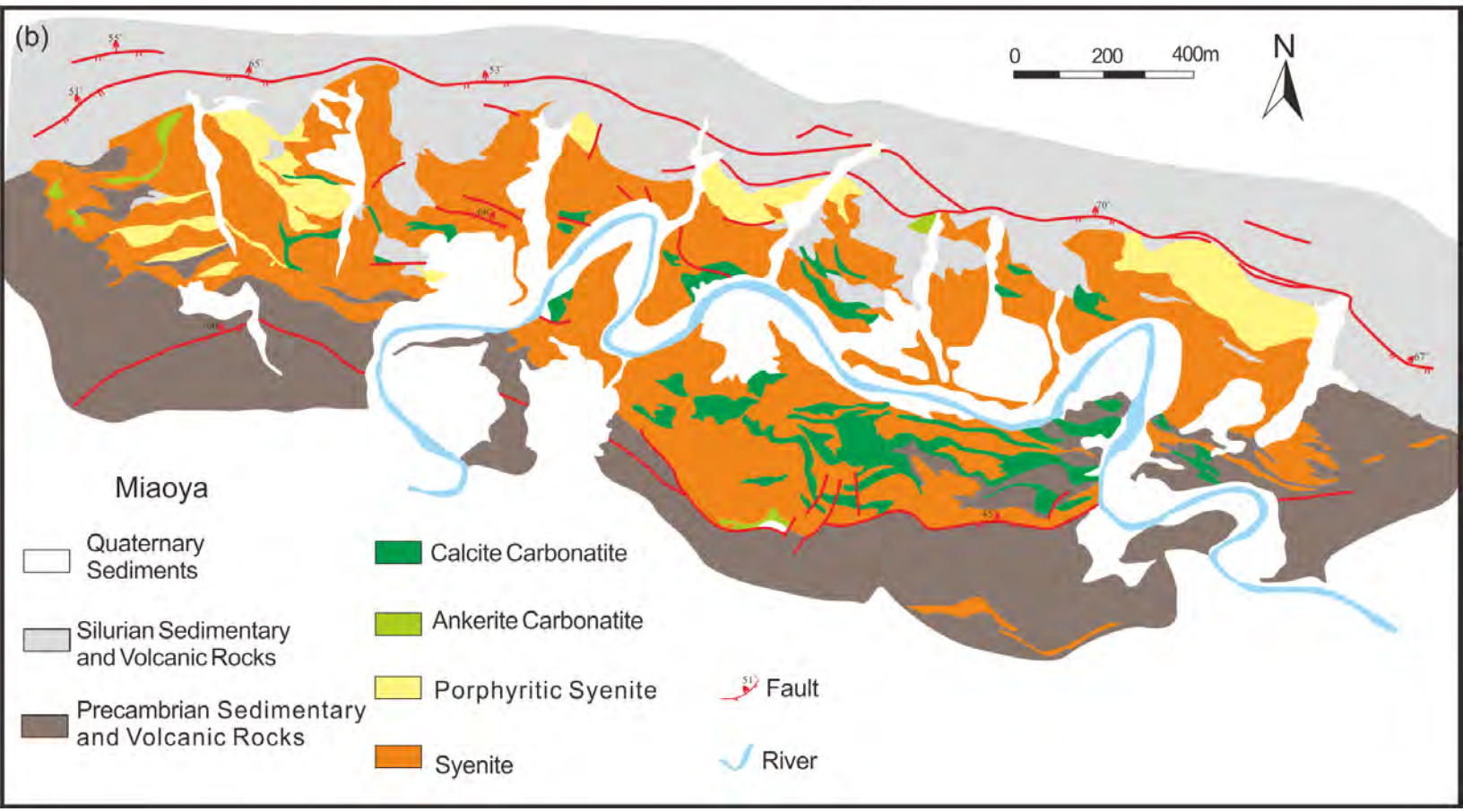

This is the peer-reviewed, final accepted version for American Mineralogist, published by the Mineralogical Society of America.
The published version is subject to change. Cite as Authors (Year) Title. American Mineralogist, in press.
DOI: https://doi.org/10.2138/am-2021-7746. http://www.minsocam.org/

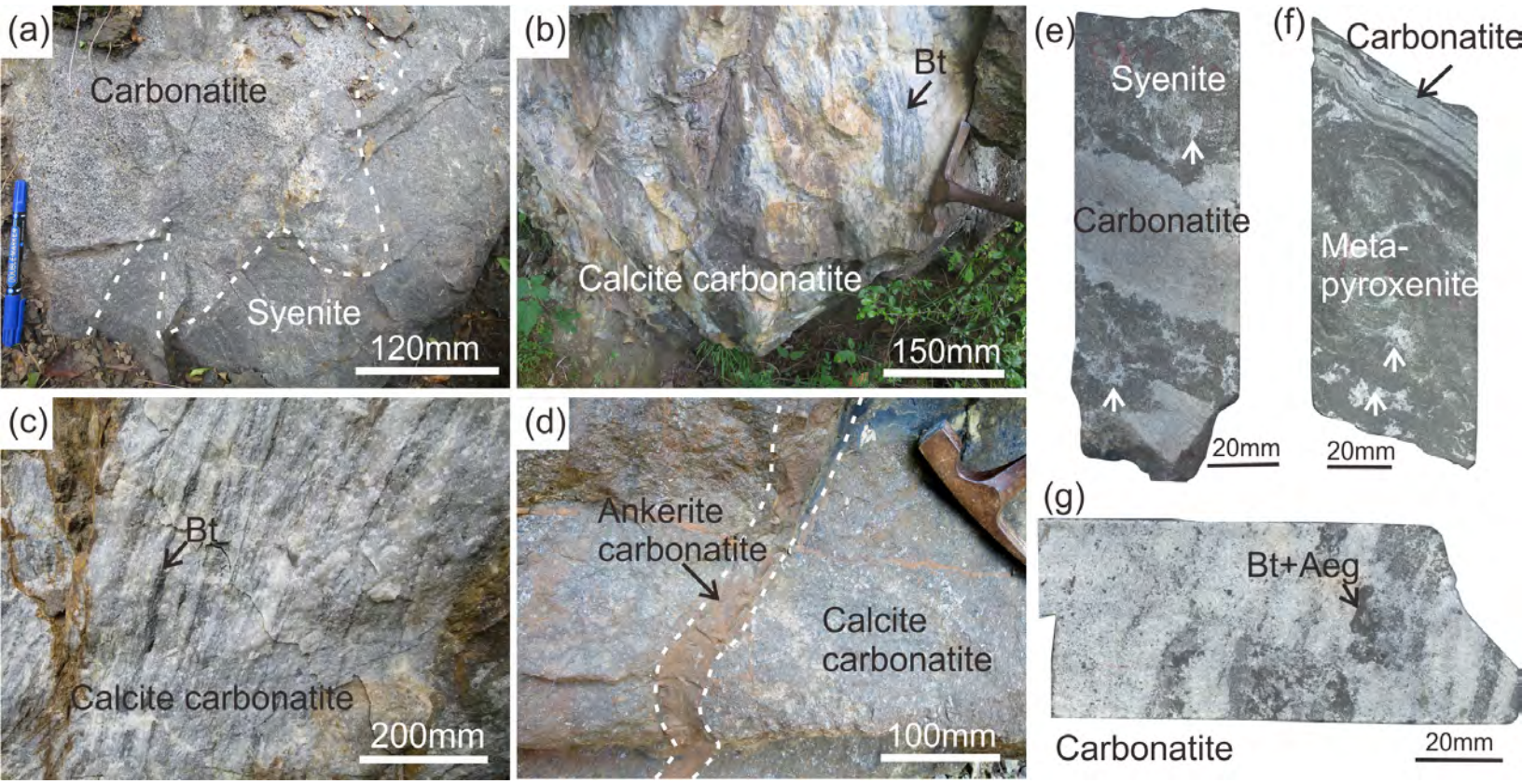

This is the peer-reviewed, final accepted version for American Mineralogist, published by the Mineralogical Society of America.
The published version is subject to change. Cite as Authors (Year) Title. American Mineralogist, in press.
DOI: https://doi.org/10.2138/am-2021-7746. http://www.minsocam.org/

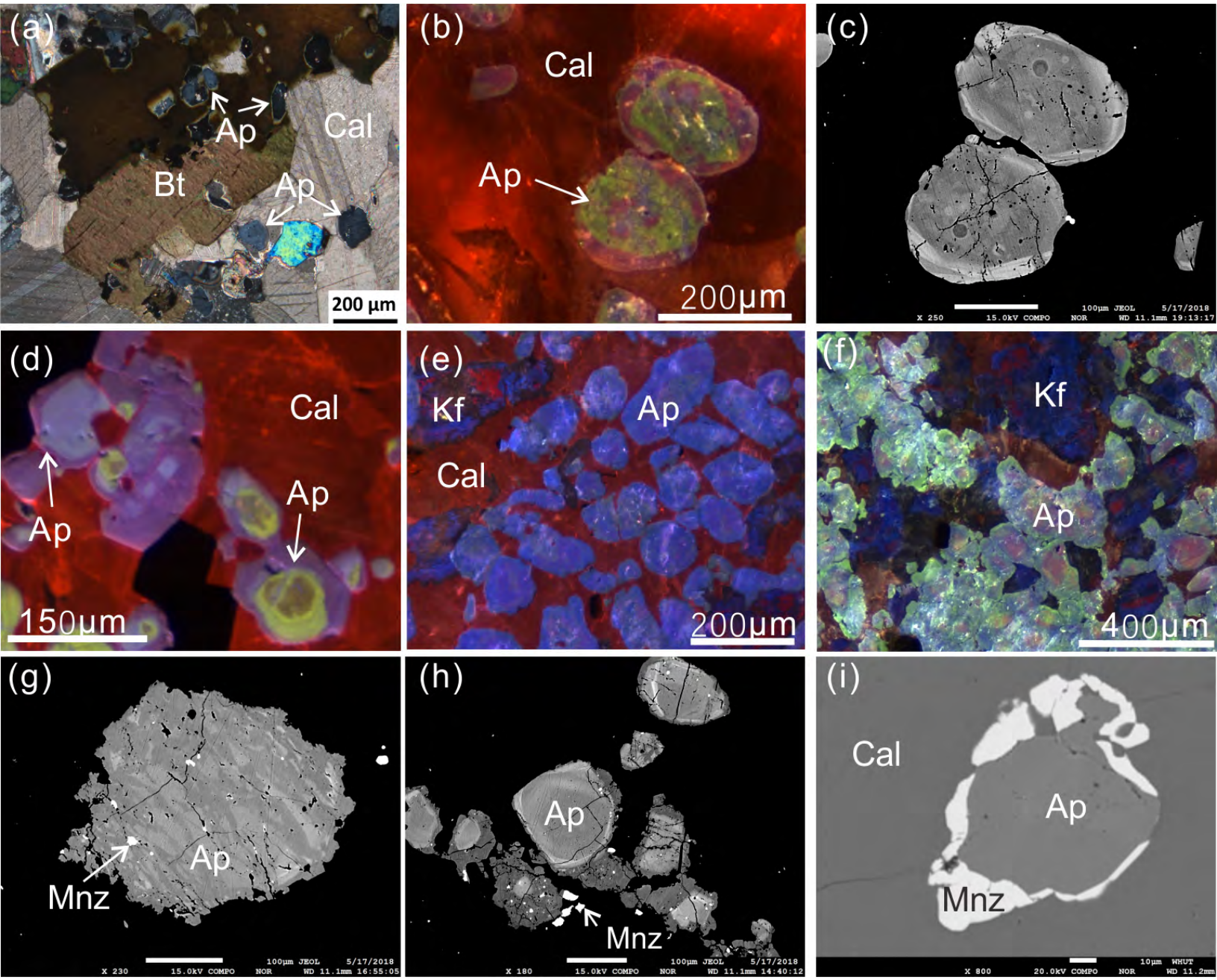

This is the peer-reviewed, final accepted version for American Mineralogist, published by the Mineralogical Society of America.
The published version is subject to change. Cite as Authors (Year) Title. American Mineralogist, in press.
DOI: https://doi.org/10.2138/am-2021-7746. http://www.minsocam.org/

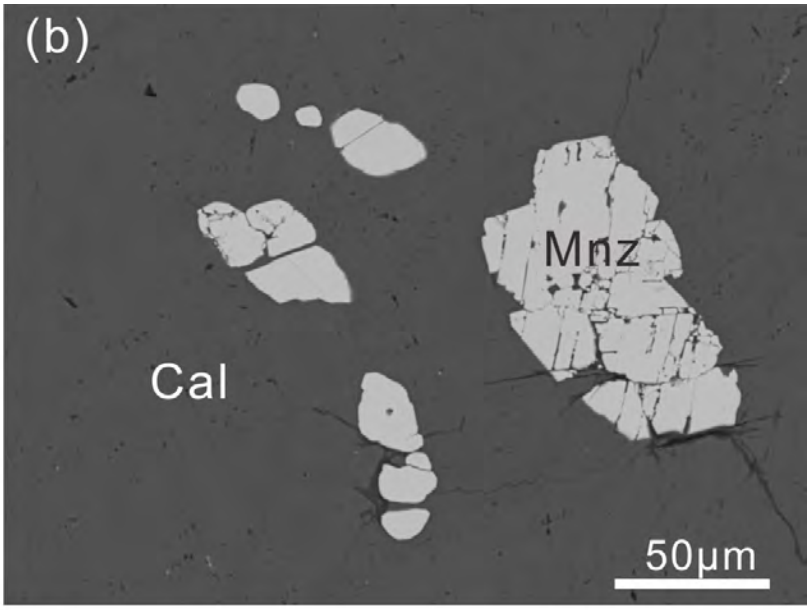

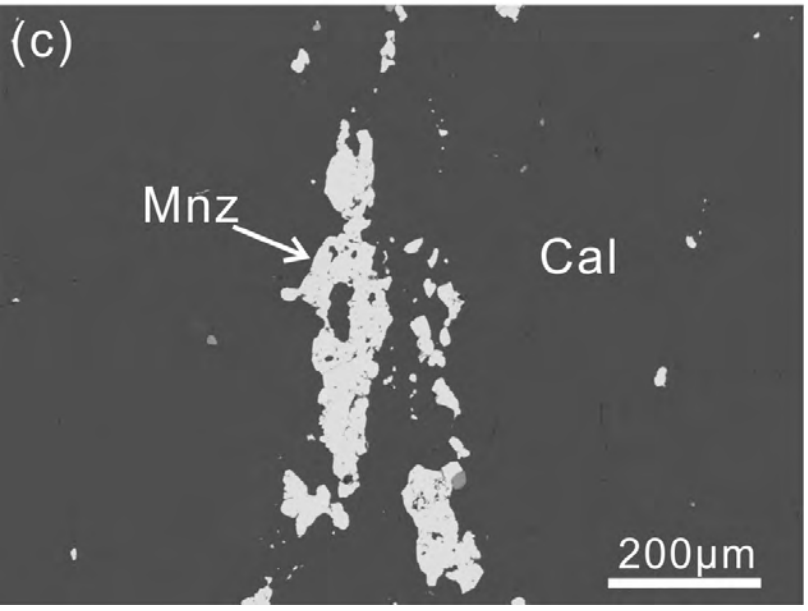

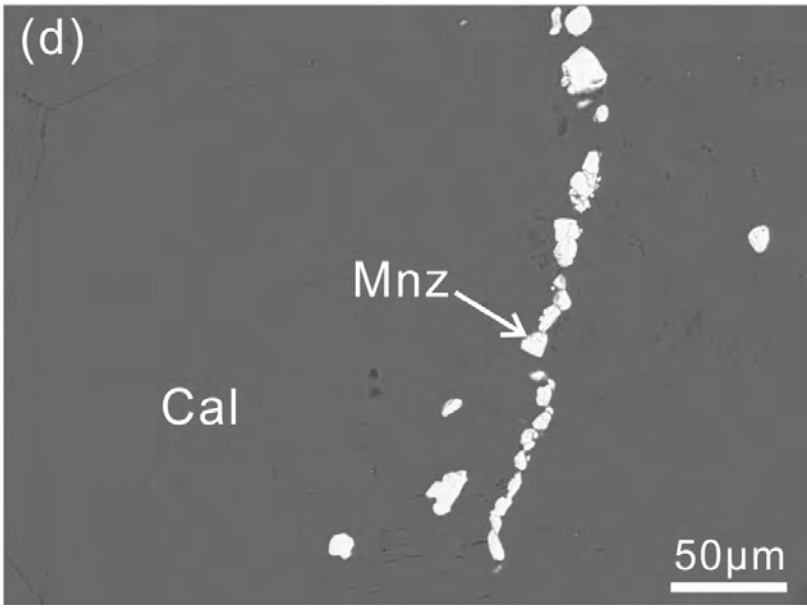

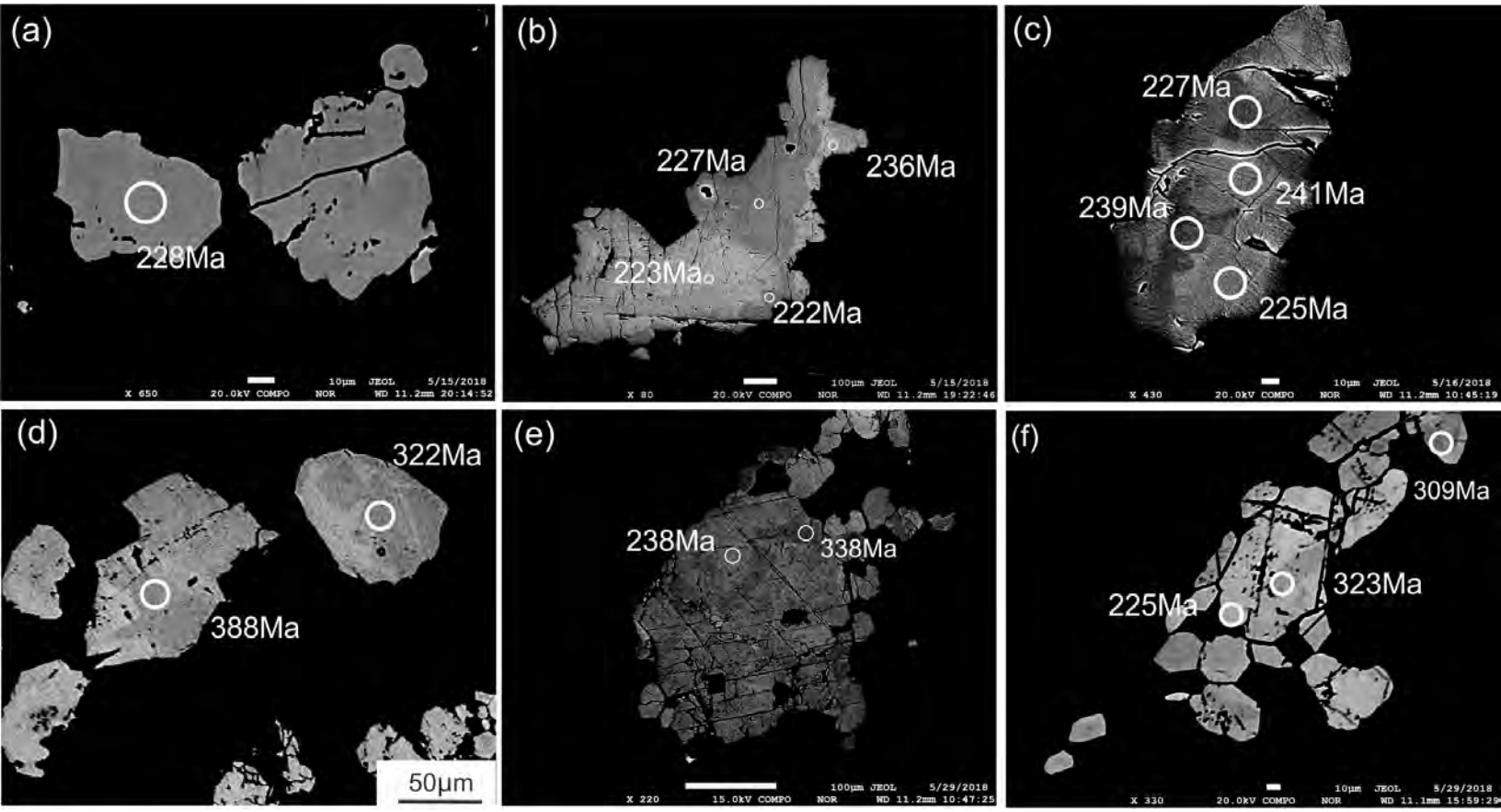

This is the peer-reviewed, final accepted version for American Mineralogist, published by the Mineralogical Society of America.
The published version is subject to change. Cite as Authors (Year) Title. American Mineralogist, in press.
DOI: https://doi.org/10.2138/am-2021-7746. http://www.minsocam.org/

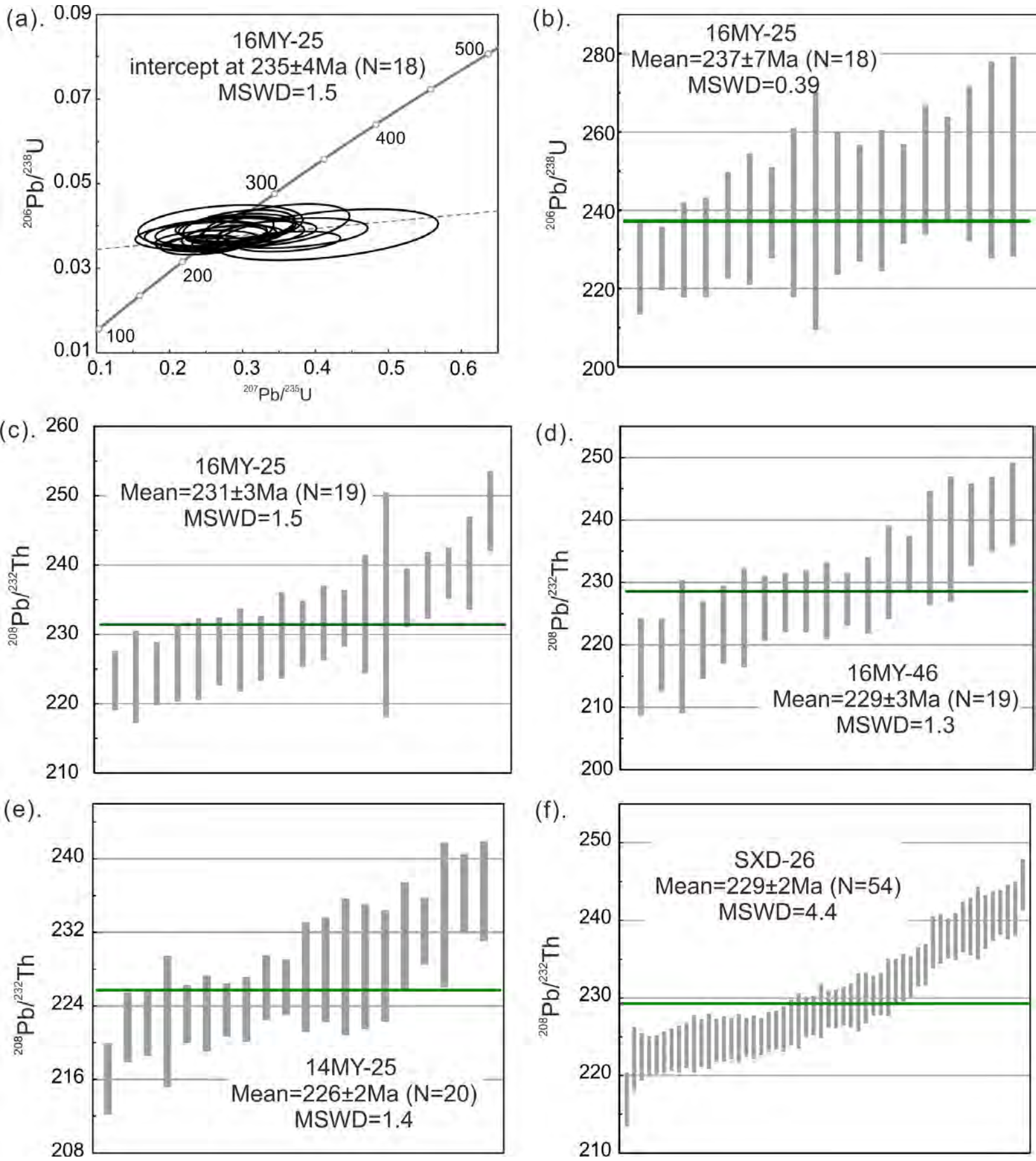

This is the peer-reviewed, final accepted version for American Mineralogist, published by the Mineralogical Society of America.
The published version is subject to change. Cite as Authors (Year) Title. American Mineralogist, in press.
DOI: https://doi.org/10.2138/am-2021-7746. http://www.minsocam.org/

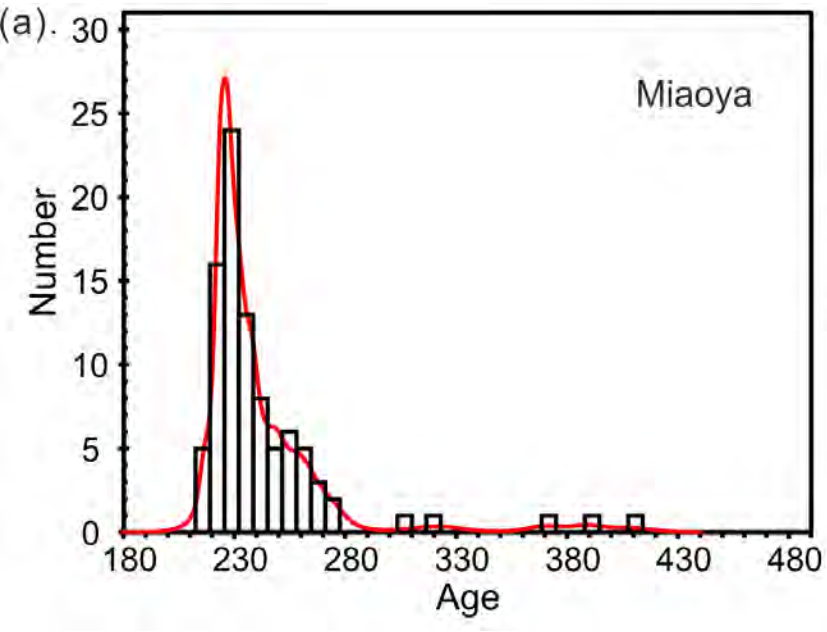

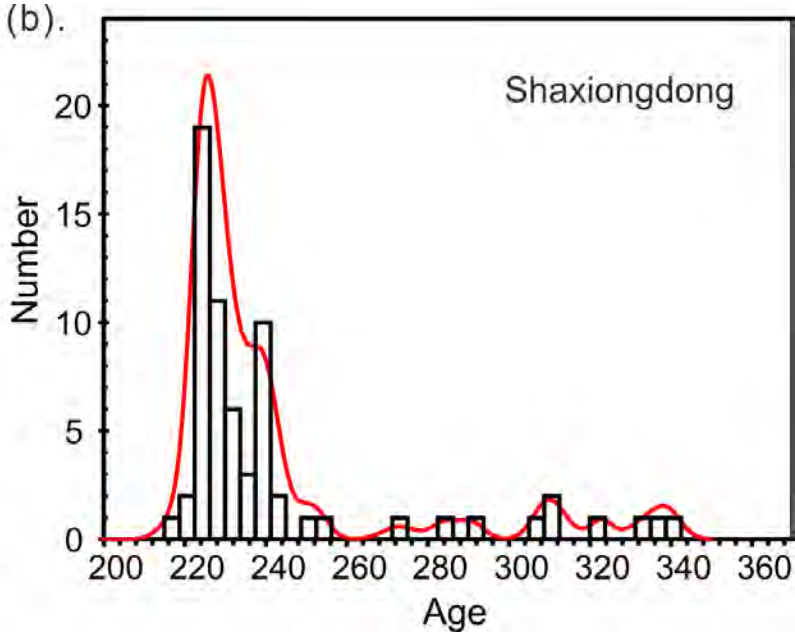

This is the peer-reviewed, final accepted version for American Mineralogist, published by the Mineralogical Society of America.
The published version is subject to change. Cite as Authors (Year) Title. American Mineralogist, in press.
DOI: https://doi.org/10.2138/am-2021-7746. http://www.minsocam.org/

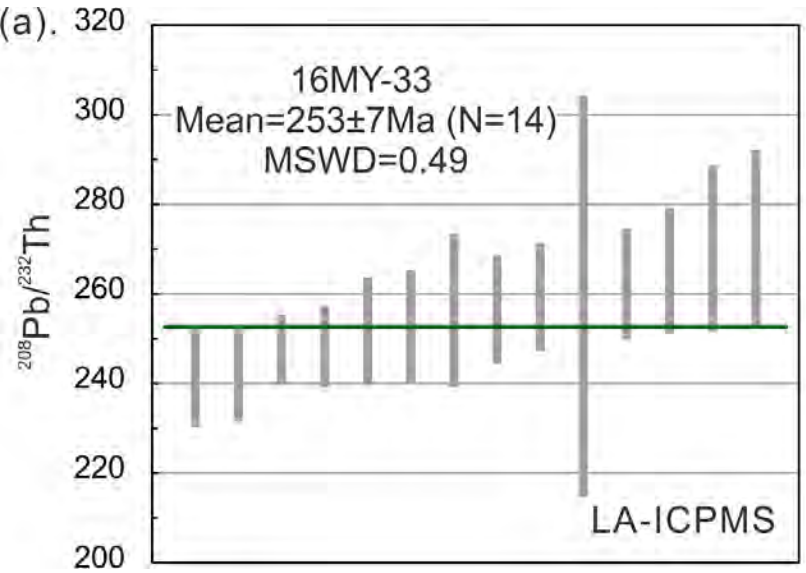

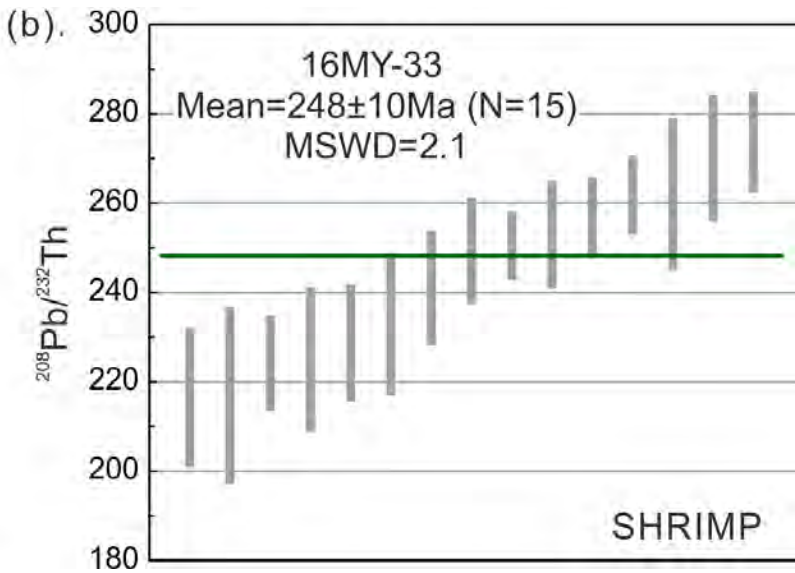

This is the peer-reviewed, final accepted version for American Mineralogist, published by the Mineralogical Society of America.
The published version is subject to change. Cite as Authors (Year) Title. American Mineralogist, in press.
DOI: https://doi.org/10.2138/am-2021-7746. http://www.minsocam.org/

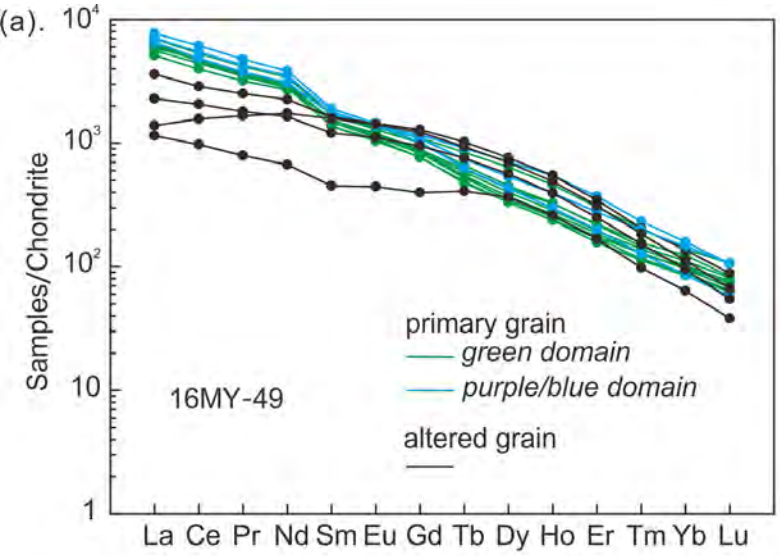

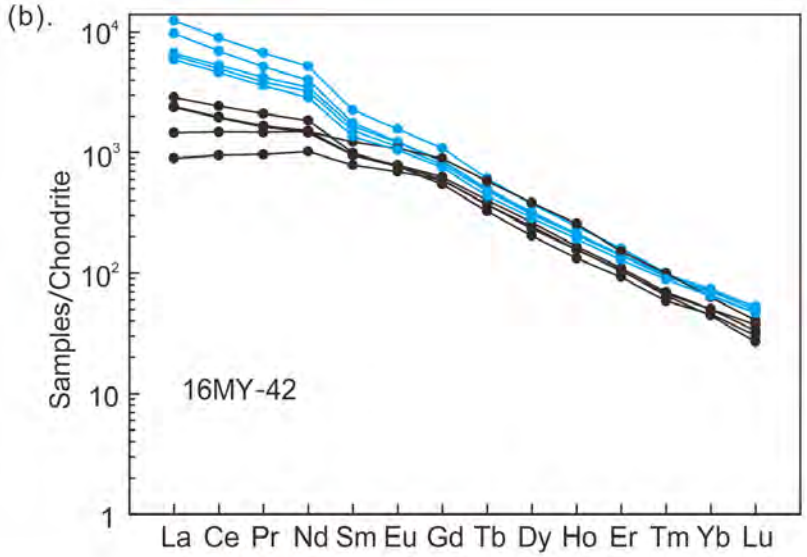

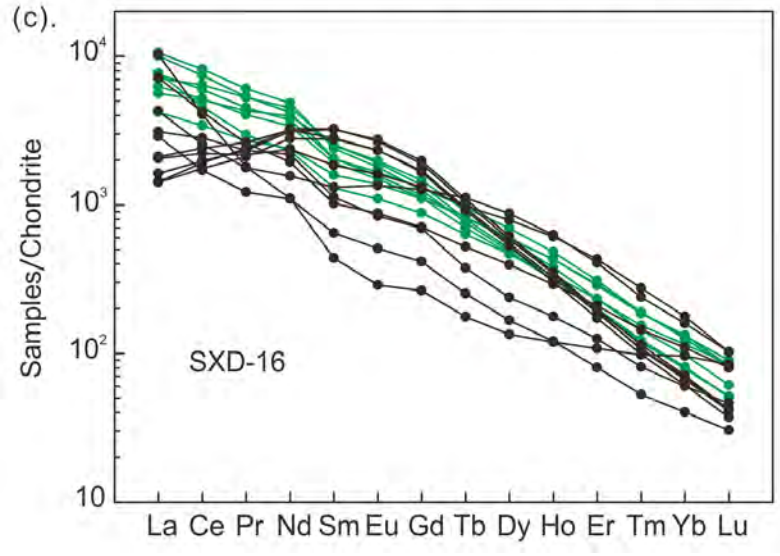

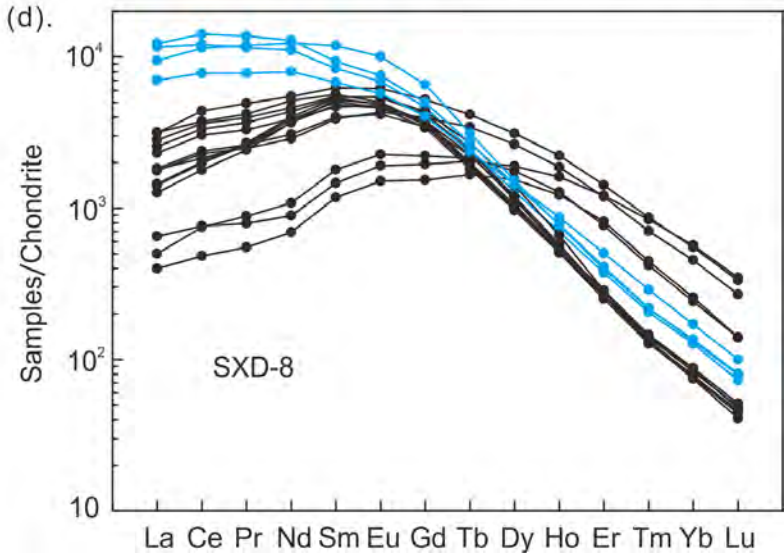

This is the peer-reviewed, final accepted version for American Mineralogist, published by the Mineralogical Society of America.
The published version is subject to change. Cite as Authors (Year) Title. American Mineralogist, in press.
DOI: https://doi.org/10.2138/am-2021-7746. http://www.minsocam.org/

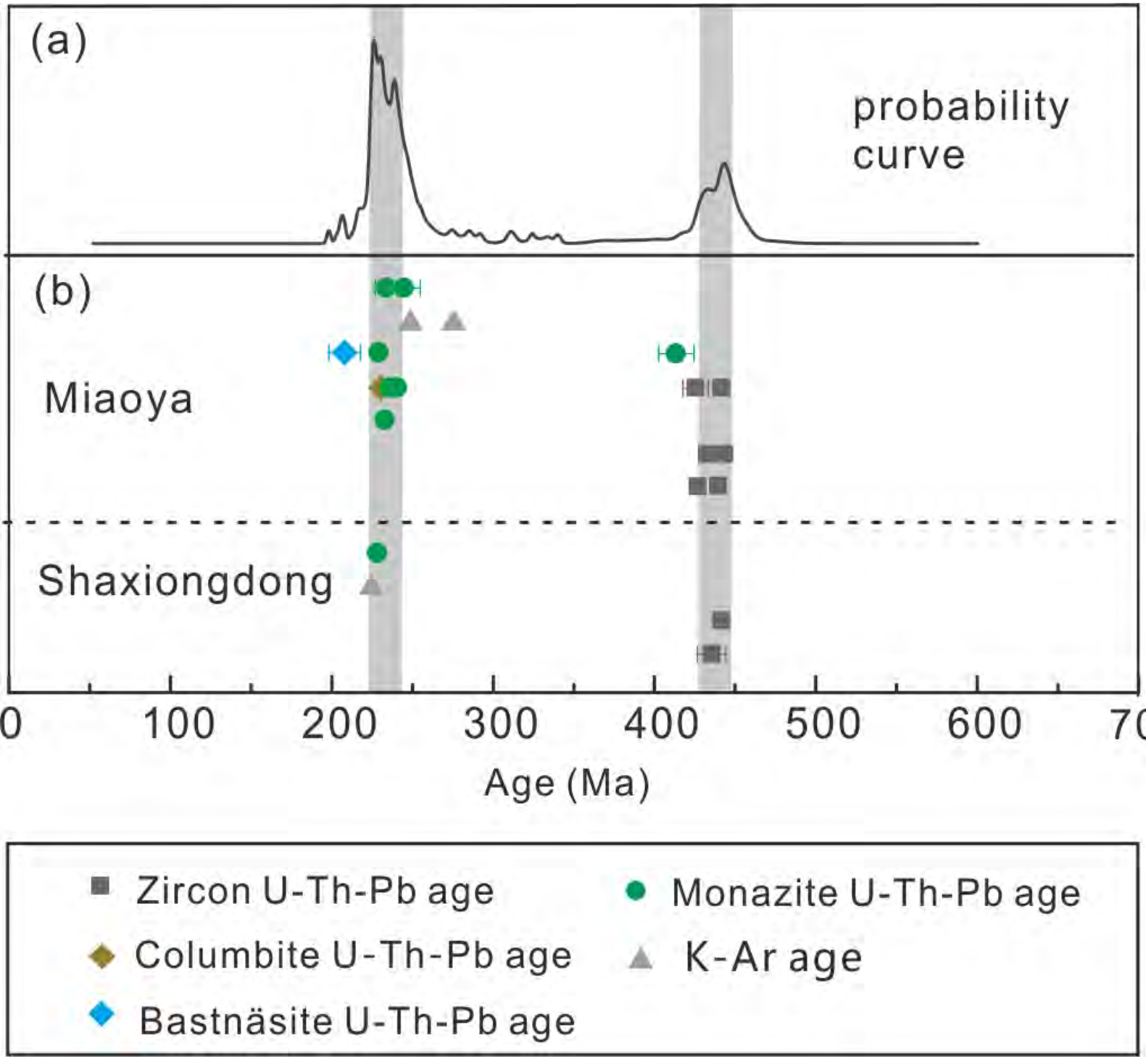

This is the peer-reviewed, final accepted version for American Mineralogist, published by the Mineralogical Society of America.
The published version is subject to change. Cite as Authors (Year) Title. American Mineralogist, in press.
DOI: https://doi.org/10.2138/am-2021-7746. http://www.minsocam.org/

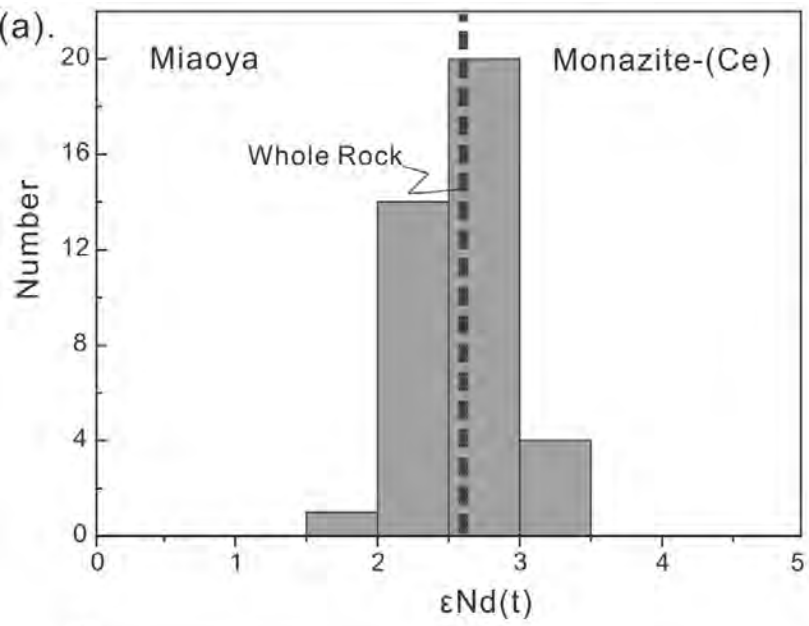

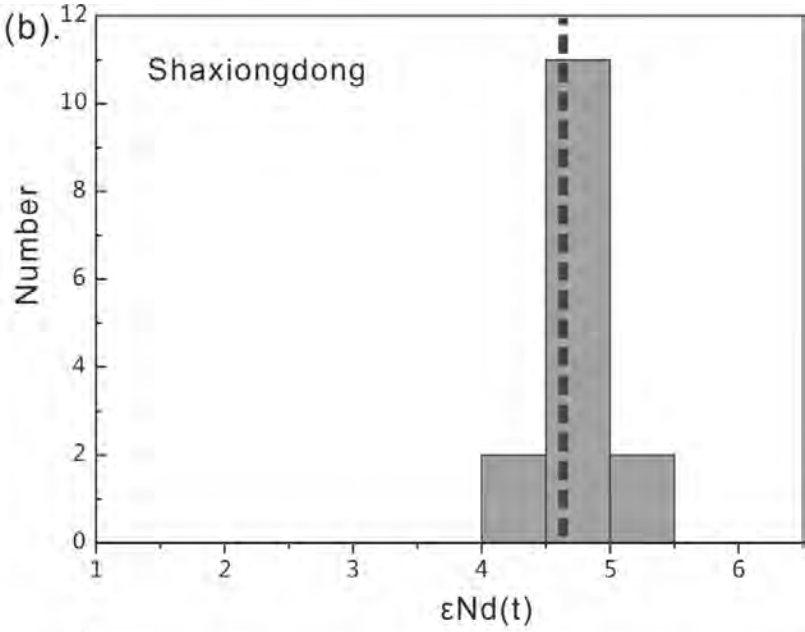

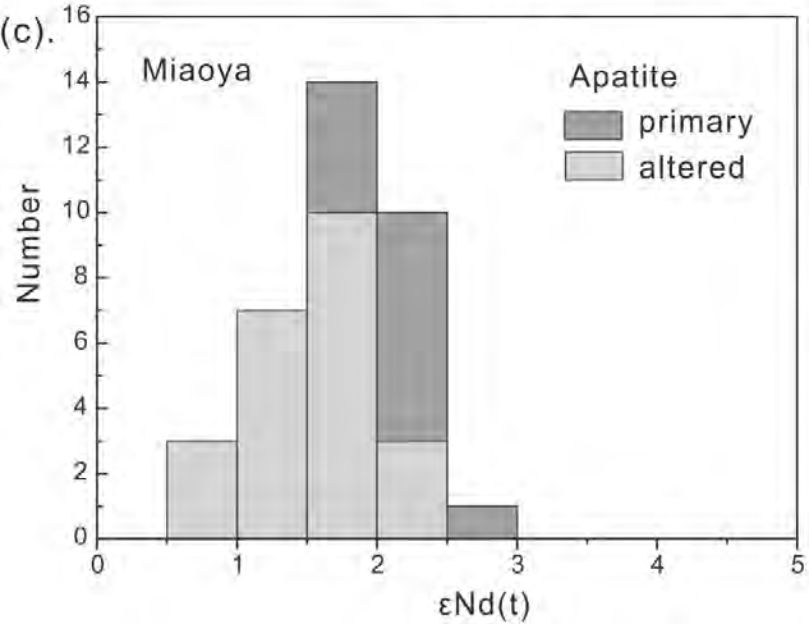

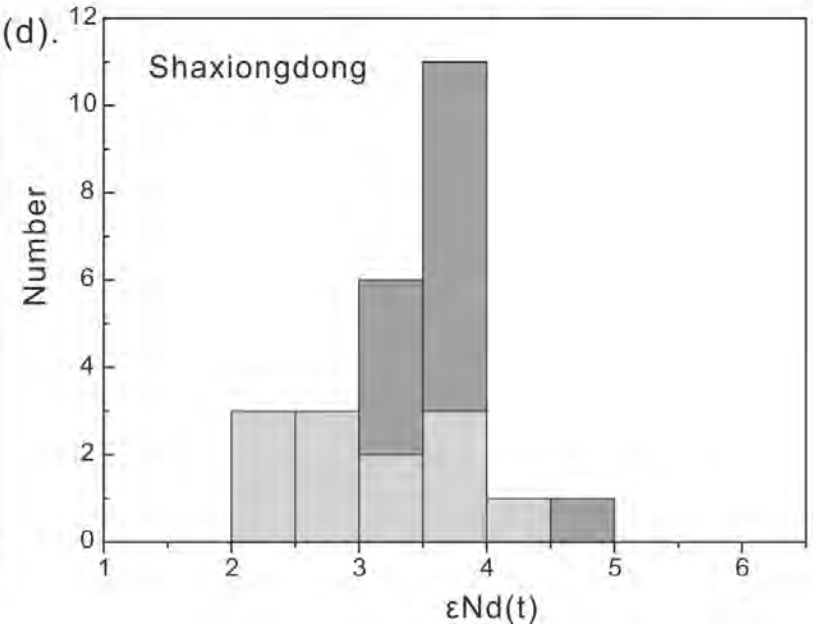

This is the peer-reviewed, final accepted version for American Mineralogist, published by the Mineralogical Society of America.
The published version is subject to change. Cite as Authors (Year) Title. American Mineralogist, in press.
DOI: https://doi.org/10.2138/am-2021-7746. http://www.minsocam.org/

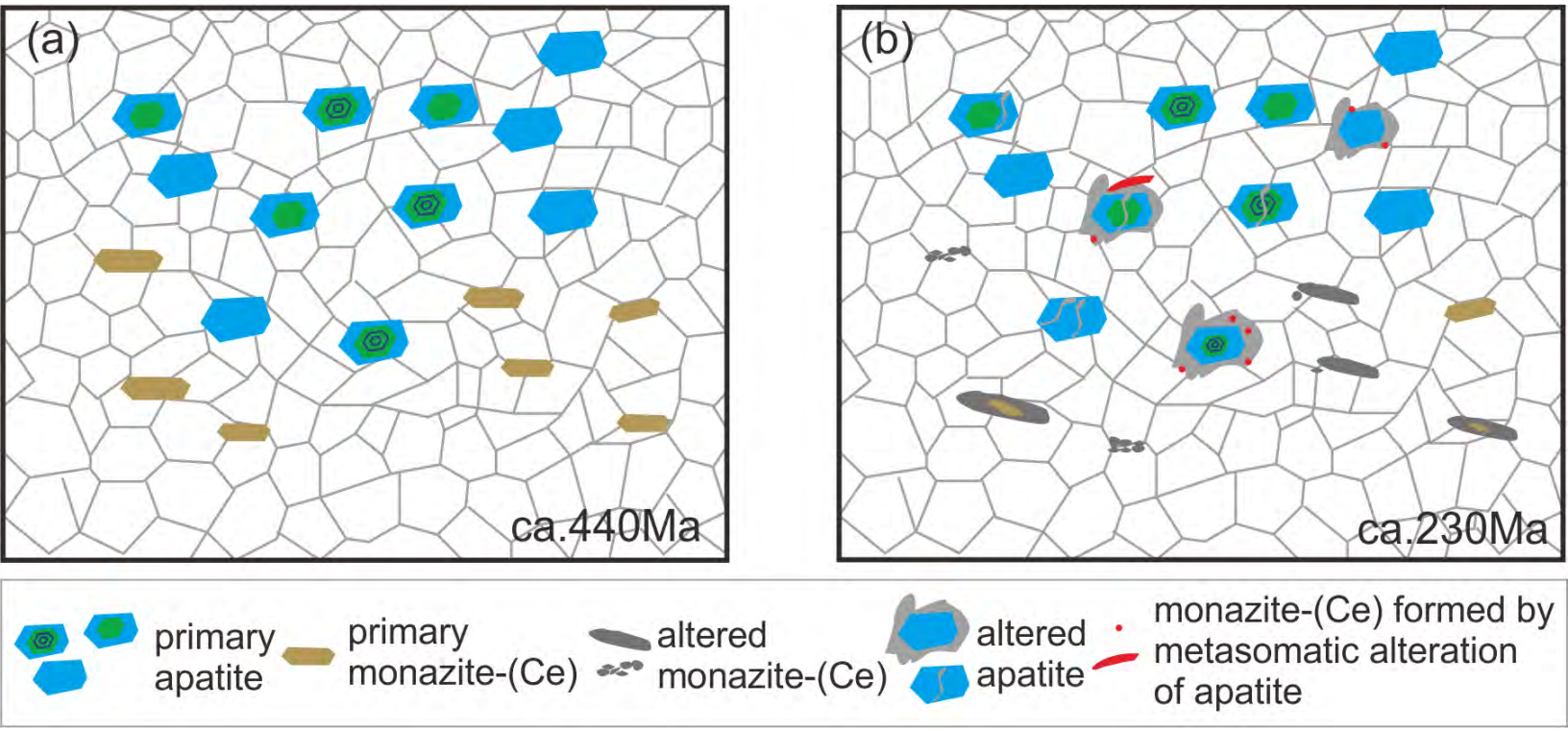

This is the peer-reviewed, final accepted version for American Mineralogist, published by the Mineralogical Society of America.
The published version is subject to change. Cite as Authors (Year) Title. American Mineralogist, in press.
DOI: https://doi.org/10.2138/am-2021-7746. http://www.minsocam.org/

Table 1. a list of studied samples.

Sample	Rock Type	Mineralogy*	Analysis
Miaoya complex			
16MY-25	carbonated syenite	Kf+Cal+Mnz+Ap	Monazite U-Th-Pb dating and Nd isotopes Apatite Nd isotopes
16MY-33	calcite carbonatite	Cal+Mnz+Bas+Par+Aln+Qz	Monazite U-Th-Pb dating and Nd isotopes
16MY-46	calcite carbonatite	Cal+ Ap+Mnz	Monazite U-Th-Pb dating and Nd isotopes Apatite Nd isotopes
14MY-25	calcite carbonatite	Cal+Mnz	Monazite U-Th-Pb dating
16MY-37	calcite carbonatite	Cal+Bt+Ap+Aln	Apatite Nd isotopes
16MY-38	calcite carbonatite	Cal+Ap+Kf	Apatite Nd isotopes
16MY-42	calcite carbonatite	Cal+Ap+Mnz	Apatite trace elements and Nd isotopes
16MY-49	calcite carbonatite	Cal+Ap	Apatite trace elements
Shaxiongdong complex			
SXD-26	calcite carbonatite	Cal+Mnz+Bas+Ap+Bar	Monazite U-Th-Pb dating and Nd isotopes
SXD-2	calcite carbonatite	Cal+Ap+Aeg+Pyr	Apatite Nd isotopes
SXD-8	carbonated syenite	Ab+Bt+Cal+Ap	Apatite trace elements
SXD-9	carbonated syenite	Ab+Bt+Cal+Ap	Apatite Nd isotopes
SXD-16	carbonated syenite	Kf+Ab+Ep+Cal+Ap	Apatite trace elements and Nd isotopes

*Ab=albite; Aeg=aegirine; Amp= amphibole; Aln=allanite; Ap=apatite; Bar=barite; Bas= bastnäsite-(Ce); Bt=Biotite; Cal=calcite; Chl=chlorite; Ep=epidote; Kf=K-feldspar; Mnz=monazite-(Ce); Par= parasite-(Ce); Pyr=pyrochlore; Qz=quartz; Ttn=titanite.